SECTION I

RESEARCH IN PROGRESS

NUCLEAR REACTIONS -- EXPERIMENTAL

MEASUREMENTS OF MOMENTUM DISTRIBUTIONS OF PROJECTILE-LIKE RESIDUES WITH THE A1200

G.A. Souliotis, D.J. Morrissey, N.A. Orr, B.M. Sherrill, and J.A. Winger

After commissioning of the A1200 beam analysis device [1] in Fall 1990, we performed a series of measurements of projectile-like residues from several beams. These measurements were a continuation of a preliminary experiment that we performed last year with the interim-vault beamline [2] and aimed at the study of the momentum distributions of near-projectile residues and especially of few nucleon pick-up products from reactions in the intermediate energy regime.

For the present measurements, the A1200 was operated as a 0-degree spectrometer in the medium acceptance mode. Fragmentation targets were placed at the beginning of the A1200. The reaction products were focused and detected at the end of the device with a detection array consisting of two X-Y sensitive PPACs and a ΔE–E telescope. The ΔE detector was a 0.5mm Si PIN diode, whereas the E detector was a 5cm-thick plastic scintillator viewed by two PMTs. The ΔE detector provided good Z separation. Adequate mass separation was obtained by measuring time-of-flight (TOF) against the RF cycle of the cyclotron (the TOF resolution was better than 2 ns). The momentum of the products was deduced by measuring their position at the second intermediate (dispersive) image of the A1200 with a third PPAC. By measuring the positions of the 0-degree elastically scattered beam particles with various charge states, a rigidity vs. position calibration was obtained. An absolute measurement of the beam rigidity was achieved by positioning a known elastic peak at the center of the dispersive-image PPAC and measuring the corresponing magnetic fields of the first pair of dipoles with their NMR readouts.

In the first experiment, we measured the near-projectile products from a ^{20}Ne beam at 85 MeV/u on Ta (10 mg/cm^2) and Be (3 mg/cm^2) targets. A series of successive steps of the fields of the A1200 was performed covering the A/q region of 2.1–3.0. In addition, we performed the same series of measurements with ^{15}N and ^{18}O beams at 70 MeV/u on Ta target.

Isotope separation and identification were performed with a two-dimensional histogram of ΔE vs. A/q (a parameter constructed by combining the RF-TOF measurement with the position measurement). Normalization of the runs using a beam current integrator was not possible, since in many runs the unreacted beam was not completely collected by the Faraday cups inside the first pair of dipoles. A relative normalization of the runs was attempted, as most of the successive runs were overlapping in rigidity by

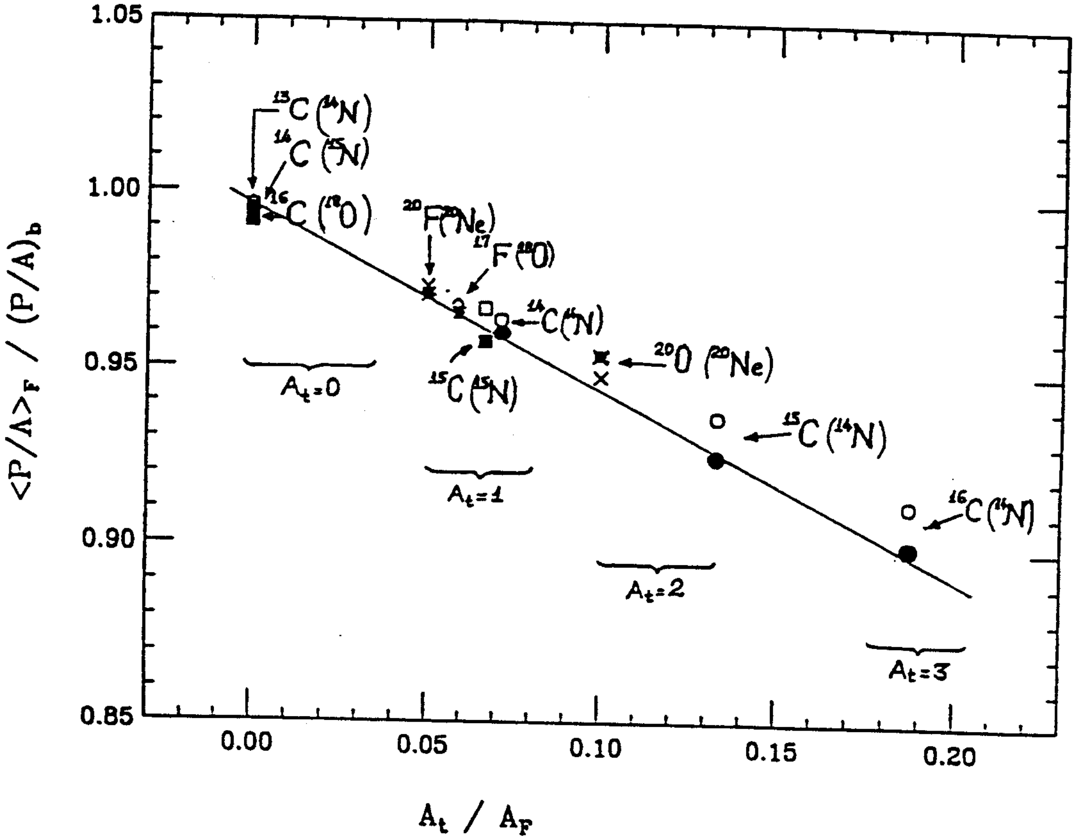

Figure 1: Variation of the centroids of the momentum distributions of few-nucleon pick-up products with the number of nucleons picked-up . For a given product, the quantity $< P/A >_F$ is the centroid of a Gaussian function used to fit the momentum-per-nucleon distribution; $(P/A)_b$ is the momentum/nucleon of the corresponding primary beam; A_t is the number of nucleons picked-up and A_F is the mass of the product. The closed symbols are the experimentally obtained values, whereas the open ones are calculated with the proposed model (see text). Each point is identified by the corresponding isotope (and in parentheses the beam it came from). The points corresponding to a ^{14}N beam (75 MeV/u, Al target), (circles) are data from our experiment with the interim vault beamline[2]. All other points are from the measurements with the A1200 and a Ta (10mg/cm^2) target. The line through the data points is drawn to guide the eye.

approximately 1%. (the field stepping was 2%, whereas the momentum acceptance of the A1200 is 3%). A few of the momentum spectra obtained from this data set (which is still under analysis) are complete. These spectra were fitted with Gaussian functions and their centroids and widths are being analysed. From these distributions, the momentum distributions of pick-up products are espesially interesting. Their centroids are considerably lower than those of the corresponding fragmentation products (Fig. 1) and their widths are larger. In order to interpret these characteristics (observed also in the results of our previous experiment with the interim vault beamline [2] (see also Fig. 1), we propose an extention of the simple picture of Goldhaber's model [3] that includes nucleon pick-up. The basic idea of the new model is the application of momentum conservation to the projectile-target system and the assumption that the nucleons picked-up from the target have preferentially momenta near the top of the Fermi sphere in the direction of the projectile motion. This picture provides a satisfactory description of the variation of the centroids with the number of nucleons picked-up . It is interesting to note that the simpler assumption that the picked-up nucleons are at rest (on average) in the target frame is not consistent with our data.

References

1. B.M. Sherrill et al., Proceedings of the 1st International Conference on Radioactive Nuclear Beams, Oct 1989, Berkeley, California, edited by W.D. Meyers, J.M. Nitschke, and E.B. Norman (World scientific, Singapore, 1990), p. 563. and B.M. Sherrill et al. NSCL Annual Report 1989, p. 200.
2. G.A. Souliotis et al., Review of Scientific Instruments 62(2), (1991), p 342 and G.A. Souliotis et al., NSCL Annual Report 1989, p. 205.
3. A.S. Goldhaber, Physics Letters 53B, (1974), p 306.

MEAN FIELD DEFLECTION IN PERIPHERAL HEAVY-ION COLLISIONS

W.K. Wilson, D.A. Cebra, S. Howden, J. Karn, D. Krofcheck, R. Lacey, T. Li, A. Nadasen, T. Reposeur, A. Vander Molen, C.A. Ogilvie, G.D. Westfall, and J.S. Winfield

The attractive component of the nuclear mean-field is expected to be increasingly important in the dynamics of heavy-ion collisions as the beam energy is decreased below ≈ 100 MeV/nucleon.[1] The first direct observation of attractive deflection by the mean-field at beam energies near the Fermi energy was made by Tsang et al. using 20 and 35 MeV/nucleon N projectiles and a Sm target.[2] Recently, several experiments have studied the role of the mean-field indirectly by examining the transverse collective motion (flow) created by attractive deflection in reactions from 35 to 100 MeV/nucleon.[3,4,5,6] Interest has focused on these experiments because of their potential for using the beam energy evolution of the collective motion to constrain the equation of state of nuclear matter.

These collective motion experiments could not directly measure the sign of the mean-field deflection, rather it was inferred from comparisons to the predictions of microscopic calculations. We have developed an analysis which reveals the sign of the deflection directly by using lightly damped projectile fragments to determine the reaction plane. This report will review the results of our analysis of proton transverse collective motion in peripheral 50 MeV/nucleon C+Au collisions.[7]

The data presented in this report was obtained using the MSU 4π Array in its initial configuration which consisted of 215 phoswich telescopes.[8] The 170 telescopes of the Main Ball were used to detect protons of energies ≥ 18 MeV at polar angles from ≈ 18° to ≈ 162° with respect to the beam axis. Projectile fragments with velocities in excess of ≈ 70% of the beam velocity were observed using 45 telescopes in a Forward Array covering polar angles from 5.5° to 18°. Mass resolution of hydrogen isotopes in the Main Ball allowed separation of protons from other light particles while projectile fragments ($3 \leq Z \leq 6$) were identified by their charge in the Forward Array.

The velocity spectra for projectile fragments observed in the Forward Array, shown in Fig. 1, exhibit peaks near the beam velocity. Since the angular acceptance for projectile fragments extends down to the grazing angle, and since the fragments are only lightly damped, we can assume that the fragments in the peak of the velocity spectra were positively deflected by the repulsive Coulomb interaction.

Using the projectile fragment to determine the reaction plane, a coordinate system (see Fig. 2) for each event was chosen such that the z axis lay along the beam axis and the positive x axis had the same

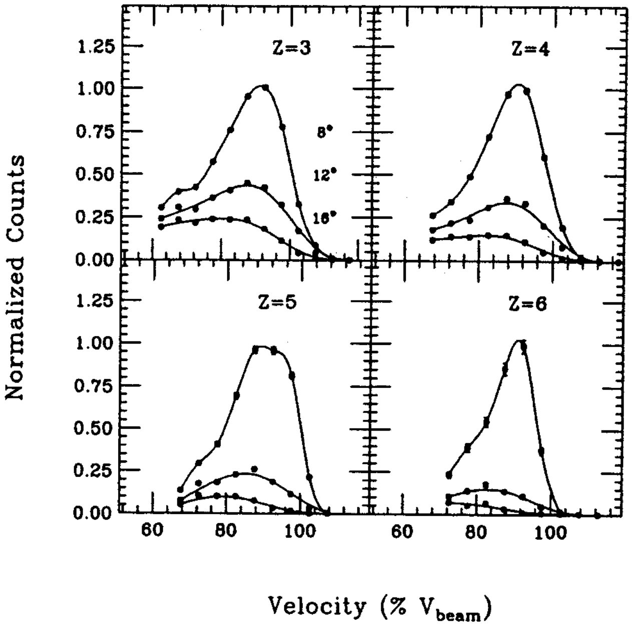

Figure 1: Velocity spectra for projectile fragments detected in the Forward Array in coincidence with protons in the Main Ball for 50 MeV/nucleon C+Au collisions.

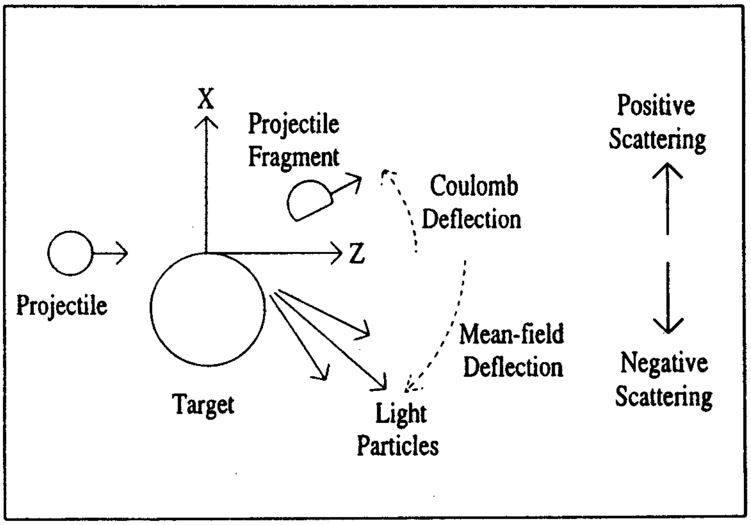

Figure 2: Coordinate system used in interpreting the correlations between projectile fragments and light particles in peripheral collisions.

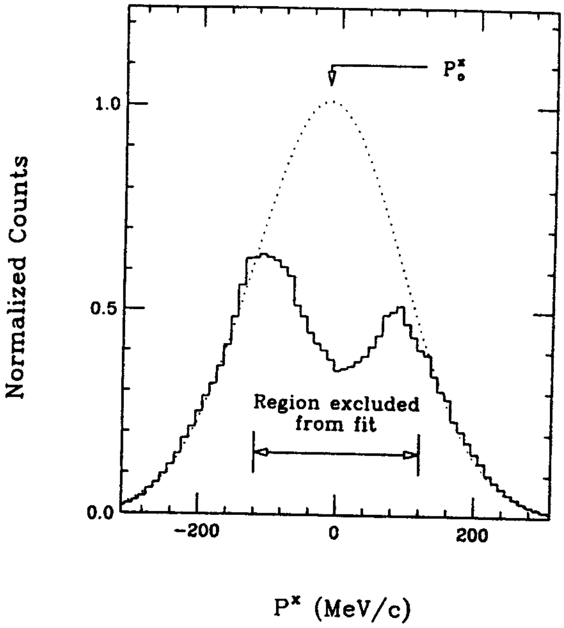

Figure 3: Histogram of the transverse momentum distribution projected on to the reaction plane for mid-rapidity protons detected by the Main Ball in 50 Mev/nucleon C+C reactions. The distribution for 50 MeV/nucleon C+Au reactions is similar. The valley around $P^x \approx 0$ MeV/c is due to detector low energy thresholds and was excluded from the Gaussian fits described in the text.

azimuthal angle as the fragment. The momentum distribution of mid-rapidity protons ($y \approx \frac{1}{2}y_{beam}$) is shown in Fig. 3 projected onto the P^x axis and smeared over the angular acceptance of the detectors. The center of the P^x distribution, P_o^x, can be found by fitting with a Gaussian distribution. Our technique for revealing the deflection of these protons is to plot the center of the P^x distribution as a function of rapidity near mid-rapidity. Except for the reaction plane determination, this is essentially the same approach used to study transverse collective motion in relativistic collisions.[9]

In the rapidity and transverse momentum region studied we expect contributions from both the mid-rapidity and projectile-like sources. Although the momentum distributions of these particles overlap somewhat, we can distinguish between these two sets of protons by noting that the energy spectrum produced by the mid-rapidity source is much harder than that due to the projectile source. In order to concentrate on the mid-rapidity source, we therefore excluded protons with a $|P^x| \leq 250 MeV/c$ from the Gaussian fits, minimizing the contribution from the relatively "cool" projectile-like source. In focusing on the protons produced by the so called "mid-rapidity" source, we do not intend to imply that they originate from a well defined thermal source, only that they can be distinguished from protons produced by the decay of the excited projectile fragment.

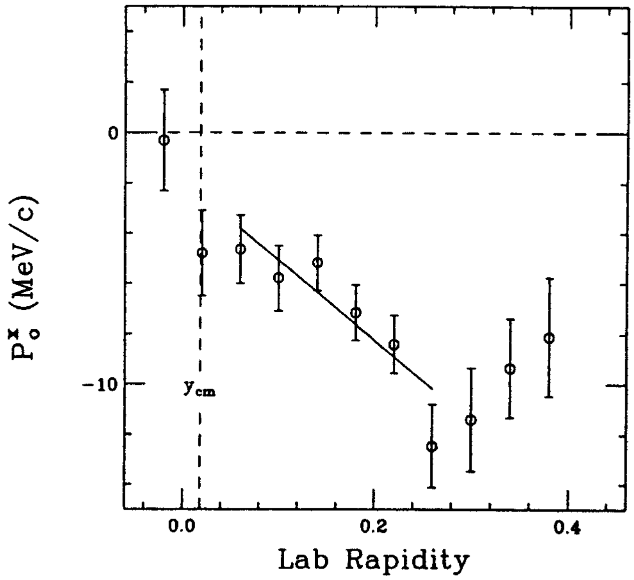

Figure 4: The center of the transverse momentum distribution in the reaction plane as a function of rapidity 50 MeV/nucleon C+Au collisions. The centers were extracted using single Gaussian fits to the high transverse momentum, mid-rapidity protons ($|P^x| \geq 250 MeV/c$) and show a negative slope at mid-rapidity (solid line).

Using this high $|P^x|$ gate, we display in Fig. 4 P_o^x vs. rapidity for the protons from the mid-rapidity source. Isolating this subset of the protons reveals a *negative* slope at mid-rapidity. A similar result was obtained in the analysis of 50 MeV/nucleon C+C reactions.[7] There is a increase in P_o^x at high rapidities in Fig. 4 that may be due to contamination from the tail of the projectile-like source distribution.

If we take the projectile fragments as being positively scattered, then the negative slope in the P_o^x distribution implies that high $P^{\perp}$ mid-rapidity protons were preferentially attractively deflected. The use of lightly damped projectile fragments to find the reaction plane may allow experimenters to observe directly the change in the sign of the deflection as the beam energy is increased from the regime in which the attractive interaction dominates to that where compressional forces take over.

References

1. G.F. Bertsch et al., Phys. Lett. 189B (1987), p 384.
2. M.B. Tsang et al., Phys. Rev. Lett. 57 (1986), p 559.
3. D. Krofcheck et al., Phys. Rev. Lett. 63 (1989), p 2028.
4. C.A. Ogilvie et al., Phys. Rev. C42 (1990), p R10.
5. W.M. Zhang et al., Phys. Rev. C42 (1990), p R491.
6. J.P. Sullivan et al., Phys. Lett. 249B (1990), p 8.
7. W.K. Wilson et al., MSU preprint MSUCL-750 (1990), submitted to Phys. Rev. C.
8. G.D. Westfall et al., Nucl. Instr. and Meth. A238 (1985), p 347.
9. P. Danielewicz and G. Odyniec, Phys. Lett. 157B (1985), p 146.

AZIMUTHAL ASYMMETRY IN AR+V COLLISIONS FROM 35 TO 100 MEV/NUCLEON

W.K. Wilson, W. Benenson, D.A. Cebra, J. Clayton, S. Howden, J. Karn, T. Li, C.A. Ogilvie, A. Vander Molen, G.D. Westfall, J.S. Winfield, B. Young, and A. Nadasen

In this report, we review our studies of azimuthal distributions in heavy-ion collisions at beam energies ranging from 35 to 100 MeV/nucleon.[1] The goal of this work is to clarify the rection mechanisms in intermediate energy collisions by investigating the relationship between modes of collective motion and observed azimuthal distributions. In contrast to relativistic collisions in which compression leads to a hydrodynamic side-splash and squeeze out,[2] collective motion the intermediate energy range under consideration is dominated by the attractive component of the nuclear mean-field.[3]

We will begin by examining the influence of two forms of collective motion, rotation and attractive flow (or mean-field deflection), on the azimuthal distributions of emitted particles. A new parameterization of the azimuthal anisotropy will be introduced which will allow us to clearly distinguish between the contributions of the different modes of collective motion. Using these parameters in the analysis of 35 MeV/nucleon Ar+V collisions, we will find that signatures of both rotation and flow are present in data taken by the MSU 4π Array. Finally, we will explore the beam energy dependence of collective motion as E_{beam} is increased to 100 MeV/nucleon.

Two distinct modes of collective motion have been proposed to explain various attributes of collisions observed in this beam energy range, rotation of the compound system and flow caused by the attractive component of the mean-field. Rotational collective motion about an axis perpendicular to the reaction plane was suggested by Tsang et al.[4] in the interpretation of two particle azimuthal correlation data. Flow, or directed transverse momentum, was invoked by Ogilvie et al.[5] to explain the dependence of average transverse momentum in the reaction plane on rapidity. In fig. 1 we illustrate the geometry of both forms of collective motion.

For the results presented in this report, the reaction plane was determined on an event by event basis from the momentum distribution of the detected particles.[1] The z-axis was chosen to lie along the beam axis. The positive x-axis was chosen to lie in the reaction plane, and by convention on the forward flow side. The forward flow side is taken as the side of the reaction plane which contains the component of the collective flow which is traveling forward in the c.m. frame of reference, as shown in fig. 1. The

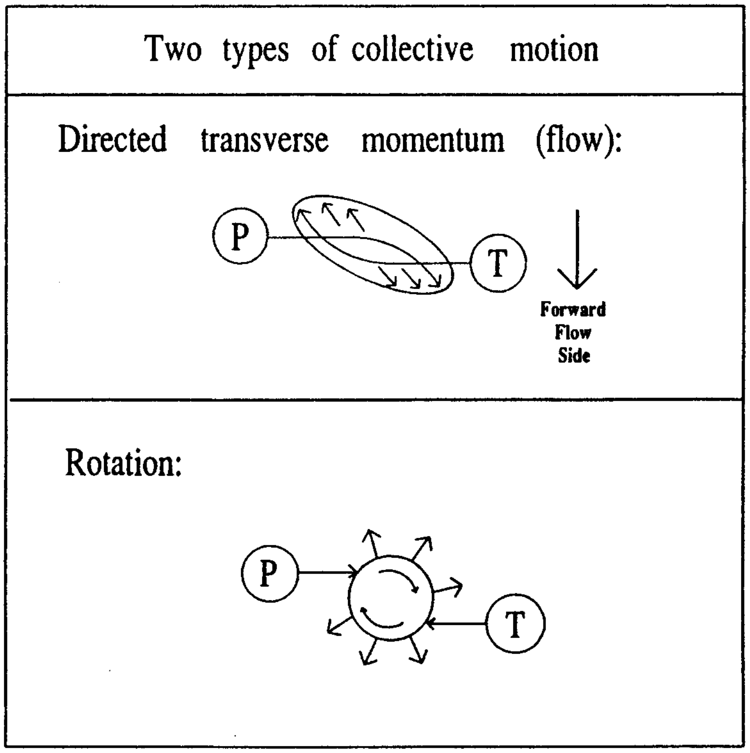

Figure 1: Schematic representation of the two forms of collective motion under investigation. Both drawings are in the center of momentum frame of reference, looking down on the reaction plane. The forward flow side of the reaction plane is the region below the dotted line in the flow picture.

azimuthal angle of a particle of interest with respect to the reaction plane was measured from the x-axis around the z-axis.

Preferential emission in the reaction plane should be observed for both rotation and flow, but the rapidity dependence is different for the two mechanisms. As can be seen from fig. 1, rotation should enhance particle emission equally on both sides of the reaction plane ($\phi = 0°, 180°$) at all rapidities. Flow, on the other hand, leads to an enhancement on one side of the reaction plane ($\phi = 0°$) for particles going forward in the center of momentum frame of reference, but on the other side ($\phi = 180°$) for particles going backward. This distinction between the two modes of collective motion allowed us to develop a parameterization that isolates the contributions of flow and rotation to the observed azimuthal asymmetries.

We found that the azimuthal distributions could be conveniently characterized by two anisotropy parameters, each chosen to be sensitive to only one form of motion. The rapidity dependence of the parameters clearly show which forms of collective motion are present and their relative strengths. The rotation sensitive parameter is F_{ip}, the fraction of particles of interest found in the reaction plane. The flow sensitive parameter is F_{fs}, the fraction on the forward flow side of the reaction plane. The fractions are calculated by integrating over the azimuthal distributions,

$$F_{ip} = \frac{\int_{-45^\circ}^{45^\circ} \frac{dn}{d\phi} d\phi + \int_{135^\circ}^{225^\circ} \frac{dn}{d\phi} d\phi}{\int_{0^\circ}^{360^\circ} \frac{dn}{d\phi} d\phi} \tag{1}$$

and

$$F_{fs} = \frac{\int_{-90^\circ}^{90^\circ} \frac{dn}{d\phi} d\phi}{\int_{0^\circ}^{360^\circ} \frac{dn}{d\phi} d\phi}. \tag{2}$$

Both fractions $= \frac{1}{2}$ if the azimuthal distribution is isotropic, indicating the absence of collective motion.

The effects of collective motion on these parameters were studied using simulated Gaussian momentum distributions. To simulate the influence of rotation, the momentum distribution was flattened into an oblate shape,

$$\sigma_x = \sigma_z > \sigma_y, \tag{3}$$

where $\hat{z}$ is along beam axis, $\hat{x}$ is in the reaction plane, and $\hat{y}$ is normal to the reaction plane. In order to simulate flow, the gaussian distribution was first stretched along the beam axis to a prolate shape, and then rotated slightly around the y axis (perpendicular to the reaction plane).

The results of the above modifications of the momentum distributions on the anisotropy fractions are displayed in fig. 2. The upper panels of the figures show F_{ip} vs. rapidity. This fraction deviates from isotropy only for the rotating source. Since flow only transfers particles from one side of the reaction plane to the other and leaves the net number in the plane unchanged, it yields an $F_{ip} = \frac{1}{2}$. On the other hand, flow produces a non-zero slope in F_{fs} since particles are deflected towards the forward flow side of the reaction plane at high rapidities and towards the opposite side at low rapidities. To summarize, an $F_{ip} > \frac{1}{2}$ is a signature of an oblate momentum distribution similar to that expected due to the decay of a rotating source, while a slope in F_{fs} as a function of rapidity indicates the presence of collective flow in the reaction plane.

Anisotropy fractions for actual 35 MeV/nucleon Ar+V collisions are shown in fig. 3 for both H and He data taken using the MSU 4π Array.[6] The transverse momentum acceptances of the detector elements was equalized by imposing software cuts. All of the features of the rotation and flow simulations are reflected in the data, suggesting the presence of both modes of collective motion.[1, 5] The presence of flow

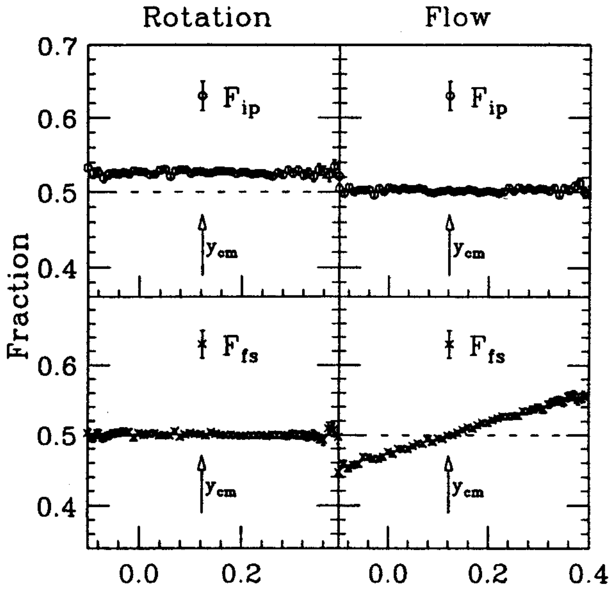

Figure 2: Anisotropy fractions F_{ip} (upper panels) and F_{fs} (lower panels) as a function of rapidity for a simulated oblate momentum distribution (left panels) and a prolate distribution with transverse momentum flow (right panels).

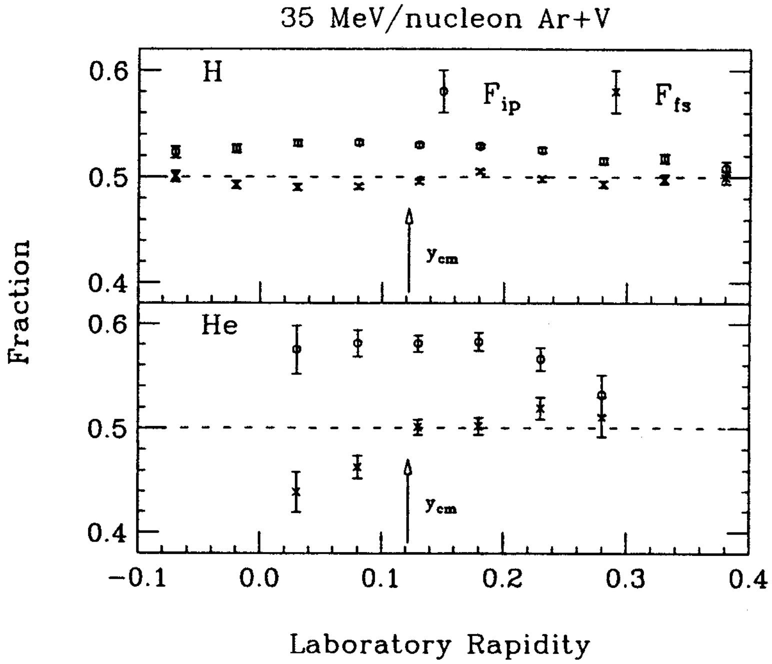

Figure 3: Anisotropy fractions as function of rapidity for 35 MeV/nucleon Ar+V data.

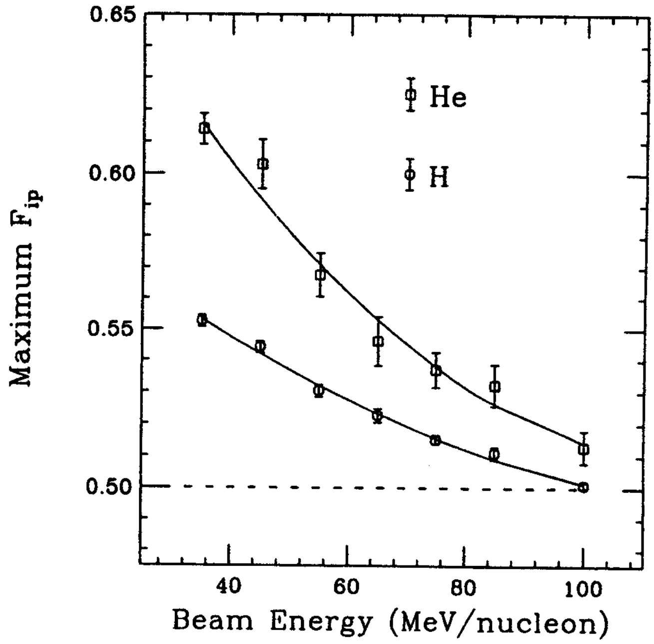

Figure 4: The maximum of F_{ip} is used to measure the oblateness of Ar+V collisions as a function of beam energy. The lines are only drawn to guide the eye.

in the collisions is revealed by fig. 3 in the non-zero slope in F_f, at mid-rapidity. The flow is stronger for helium than for hydrogen, a trend that would be expected for a collective velocity superimposed on random thermal motion. This is because thermal velocities decrease with increasing mass of the particles, leading to less random smearing of the collective velocity for helium than for hydrogen. The signature of oblateness in the momentum distribution of emitted particles, $F_{ip} > 0.5$, is particularly clear, suggesting rotational collective motion may be present. Again, the effect is stronger He than for H ions.

As the beam energy is increased to 100 MeV/nucleon, the collisions produce much more azimuthally symmetric distributions of light particles. In fig. 4, the maximum F_{ip} from the unsmeared data is presented as a function of beam energy. The detector thresholds were not modified as described earlier for the extraction of these maxima. Since the multiplicity of the events increases with the beam energy, we would expect that our ability to determine the reaction plane would improve given the same amount of collective motion. Thus, this beam energy trend is not an artifact of the accuracy of the reaction plane determination.

In summary, we find simultaneous signatures of both rotation and collective flow in our 35 MeV/nucleon Ar+V data. Both phenomena reflect the attractive nature of the nuclear mean-field as nucleons are deflected around or orbit the center of mass of the compound system. When the beam energy increases, the higher densities reached cause the repulsive component of the mean-field to dominate. Pauli blocking of collisions also lessens, and the increased energy and collisions can be expected to shorten the lifetime of the system. The near disappearance of the in-plane enhancement at $E_{beam} \approx 100$ MeV/nucleon reflects these changes in reaction mechanisms, and thus may provide a useful test for microscopic models.

References

1. W.K. Wilson et al., Phys. Rev. C41 (1990), p R1881.
2. H.H. Gutbrod et al., Rep. Prog. Phys. 52 (1989), p 1267.
3. M.B. Tsang et al., Phys. Rev. Lett. 57 (1986), p 559.
4. M.B. Tsang et al., Phys. Lett. 148B (1984), p 265.
5. C.A. Ogilvie et al., Phys. Rev. C40 (1989), p 2592.
6. G.D. Westfall et al., Nucl. Instr. and Meth. A238(1985), p 347.

OBSERVATION OF A MINIMUM IN COLLECTIVE FLOW FOR $Ar + V$ COLLISIONS

D. Krofcheck, D.A. Cebra, M. Cronqvist, R. Lacey, T. Li, C.A. Ogilvie,
A. Vander Molen, K. Tyson, G.D. Westfall, W.K. Wilson, and J.S. Winfield

It is believed that the observation of collective flow produced by collisions between heavy-ions may provide a means to characterize the nuclear equation-of-state (EOS).[1] Collective flow occurs when the measured average in-plane transverse momentum is in opposite directions for nuclear fragments emitted in the forward and backward center-of-mass hemispheres. Earlier work[2,3,4] has shown that variations in flow as a function of beam energy reflect the competition between attractive and repulsive scatterings in the intermediate beam energy regime. The beam energy at which the strengths of these scatterings are approximately balanced (E_{bal}) can be predicted by calculations with the Boltzmann-Uehling-Uhlenbeck (BUU) model[5] which incorporate the EOS via the nuclear compressibility. This would permit a direct comparison to be made between the empirically determined balance energy and that predicted by different models of the EOS.

In our previous work[2], it was observed that the collective flow diminished towards zero for the $^{40}Ar +^{51} V$ system as the beam energy was increased from 45 to 85 MeV/nucleon. This allowed the determination of a lower limit of $E_{bal} > 76$ MeV/nucleon for the energy at which the repulsive and attractive scatterings are balanced for the $^{40}Ar +^{51} V$ system. We have extended that study to a higher beam energy in an attempt to define more accurately the balancing energy. In this work we report on the measurement of the average in-plane transverse momentum for the reaction $^{40}Ar +^{51} V$ at a beam energy of 100 MeV/nucleon.

The experiment was performed using a beam of $^{40}Ar^{16+}$ ions from the K1200 cyclotron of the National Superconducting Cyclotron Laboratory incident on a 3 mg/cm^2 vanadium target. Charged, light fragments were detected with the phase I configuration of the Michigan State University 4π array.[6] This configuration consists of 215 phoswich detectors; 45 in a forward array spanning laboratory polar angles of 7^o-20^o, and 170 in the main ball between 20^o-160^o. Together, the solid angle subtended by the detectors is 85% of 4π. Isotopic resolution for hydrogen was achieved in the main ball phoswich detectors and Z resolution was obtained for all detectors.

Peripheral collisions were suppressed on the basis of the measured mid-rapidity charge[7,8] (Z_{mr}).

The Z_{mr} gates used in this work are the same as those in our earlier work.[2] Also, as discussed in ref. 8 the components of the detected fragment momentum vectors perpendicular to the beam direction were rescaled to correct for momentum conservation effects. Reaction planes were then determined for each central collision using a method developed by Wilson et al.[9] based upon the original Q-vector technique of Danielewicz and Odyniec.[10] The data were analyzed by first determining the average value of the fraction of a fragment's in-plane (p^x) to total ($p^\perp$) transverse momentum yielding $< p^x/p^\perp >$ as a function of y, the fragment's center of mass rapidity. We define the reduced flow to be $d < p^x/p^\perp > /dy$ in the region $0 < y_{cm} < 0.8 y_{proj}$ where y_{cm} is the rapidity of the fragment in the center-of-mass, and y_{proj} is the center-of-mass projectile rapidity.

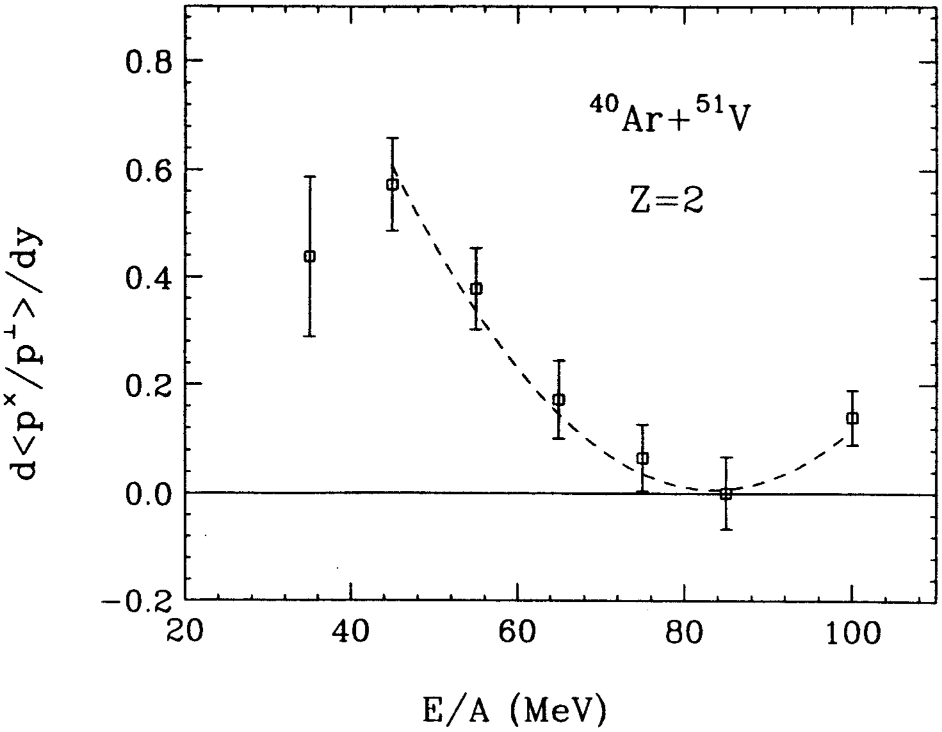

Figure 1: Reduced flow excitation function for $Z = 2$ fragments from the $^{40}Ar + ^{51}V$ reaction. The dotted line is the result of a simultaneous least-squares fit of a parabola through the excitation functions for p,d,t, $Z = 2$ and $Z = 3$ with a balance energy of 85 MeV/nucleon. The error bars are from two sources; (a)statistical accuracy of determining the slope of a line through the forward hemisphere fractional in-plane transverse momentum data, and (b)variations in the rapidity region used in fitting the straight line.

The flow at E=100 MeV/nucleon was extracted for p, d, t, $Z = 2$ and $Z = 3$ fragments and is presented for $Z = 2$ fragments in Fig. 1 along with the lower beam energy measurements of the flow excitation functions from our previous work.[2] There is evidence of the reappearance of flow at the highest beam energy. This phenomenon is expected because the empirical definition of the in-plane transverse momentum cannot distinguish between attractive and repulsive reaction mechanisms.[11] At lower beam energies, e.g. 35 MeV/nucleon, the non-zero flow is attributed to mainly attractive scatterings.[12] As the beam energy is raised from 45 to 85 MeV/nucleon, attractive scattering of fragments may become balanced by the buildup of pressure in the target and projectile overlap region and the increasing importance of individual N-N scatterings.[3] The result is the gradual disappearance of flow. At beam energies near 100 MeV/nucleon, the repulsive scattering dominates and directed, collective motion away from the interaction region occurs, resulting in the reappearance of flow. The flow excitation functions for p, t and $Z = 3$ do not show a clear non-zero flow at 100 MeV/nucleon. However, the estimated uncertainties in the data points do not rule out the reappearance of flow at this beam energy. The small magnitude of flow observed at 100 MeV/nucleon indicates that repulsive scattering does not strongly dominate the reaction mechanism.

Guided by the shape of the excitation functions which give the strongest indication of the reappearance of flow (deuterons and $Z = 2$ fragments) it is possible to estimate E_{bal} for the ${}^{40}Ar + {}^{51}V$ system. The data were fit simultaneously with various fixed E_{bal} values and assuming parabolic line-shapes. Each light-fragment fit received equal weighting in determining the overall χ^2 for a fixed balance energy. Overall minimum χ^2 from the simultaneous fits was generated for E_{bal} values of (85 ± 10) MeV/nucleon. The dotted line in Fig. 1 represents the results of the simultaneous fits for the 85 MeV/nucleon balance energy. E_{bal} is taken as the abscissa of the minimum point of the fitted parabola. The offset of this minimum from the flow zero-lines can be attributed to the finite detector sizes and to the slight influence of impact-parameter averaging over the Z_{mr} gates. It is found from individual fits that for deuterons $E_{bal} = (81 \pm 6)$ MeV/nucleon and for $Z = 2$ $E_{bal} = (84 \pm 7)$ MeV/nucleon. The errors arise from statistical limitations of the fractional in-plane transverse momentum data, changes in the boundary of the rapidity region over which flow is defined, and from variations in the assumed analytical form of the fitting function. These results are consistent with the notion that the flow observed for different fragment types may exhibit similar E_{bal} values.[2] This is an important consideration if one wishes to compare empirical E_{bal} values with theoretical predictions based upon models which do not include a clustering mechanism.

We have measured the reduced flow as a function of rapidity for light fragments from collisions of ${}^{40}Ar + {}^{51}V$ at a beam energy of 100 MeV/nucleon. Previously we have reported that collective flow seems to disappear at an incident energy above 76 MeV/nucleon[2] from measurements of collective flow using 35 to 85 MeV/nucleon ${}^{40}Ar + {}^{51}V$ data. In that work the flow was observed to decrease towards zero as the beam energy was increased from 45 to 85 MeV/nucleon. The energy at which collective flow is consistent with zero indicates the region where attractive scattering, dominant at low incident energies, is becoming balanced by the repulsive scattering observed at high energies. The point at which the the two types of scattering mechanisms are balanced (E_{bal}) may be understood as the energy at which there is a change in sign of the scattering angle.[4] At 100 MeV/nucleon there is clear evidence for the reemergence of collective flow for deuterons and $Z = 2$ fragments in the $^{40}Ar + ^{51}V$ system. The observation of a clear signal for flow enables us to determine E_{bal} for this system rather than set a lower limit as was possible with our previous data. A simultaneous least-squares fit of the data assuming parabolic line-shapes yields $E_{bal} = (85 \pm 10)$ MeV/nucleon for this system.

References

1. C.Gale, G.M. Welke, M. Prakash, S.J. Lee and S. Das Gupta; Phys. Rev. C41 (1990), p 1545.
2. C.A. Ogilvie, W. Bauer, D.A. Cebra, J. Clayton, S. Howden, J. Karn, A. Nadasen, A. Vander Molen, G.D. Westfall, W.K. Wilson, and J.S. Winfield, Phys.Rev. C42 (1990), p R10.
3. G.F. Bertsch, W.G. Lynch and M.B. Tsang, Phys. Lett. 189B (1987), p 384.
4. J.J. Molitoris, D. Hahn and H. Stöcker, Nucl.Phys. A447 (1985), p 13c.
5. G.F. Bertsch and S. Das Gupta, Physics Reports 160 (1988), p 189.
6. G.D. Westfall, J.E. Yurkon, J. van der Plicht, Z.M Koenig, B.V. Jacak, R. Fox, G.M. Crawley, M.R. Maier, B.E. Hasselquist, R.S. Tickle and D. Horn, Nucl. Inst. Meth. A238 (1985), p 347.
7. C.A. Ogilvie, D.A. Cebra, J. Clayton, S. Howden, J. Karn, A. Vander Molen, G.D. Westfall, W.K. Wilson and J.S. Winfield, Phys. Rev. C40 (1989), p 654.
8. C.A. Ogilvie, D.A. Cebra, J. Clayton, P. Danielewicz, S. Howden, J. Karn, A. Nadasen, A. Vander Molen, G.D. Westfall, W.K. Wilson, and J.S. Winfield, Phys. Rev. C40 1989), p 2592.
9. W.K.Wilson, D.A. Cebra, J. Clayton, S. Howden, J. Karn, T. Li, C.A. Ogilvie, A. Vander Molen, G.D. Westfall, B. Young, A. Nadasen and J.S. Winfield, Phys. Rev. C41 (1990), p R1881.
10. P. Danielewicz and G. Odyniec, Phys. Lett. 157B (1985), p 146.
11. D. Krofcheck, W. Bauer, G.M. Crawley, C. Djalali, S. Howden, C.A. Ogilvie, A. Vander Molen, G.D. Westfall, W.K. Wilson, R.S. Tickle and C. Gale, Phys. Rev. Lett. 63 (1989), p 2028.
12. M.B. Tsang, R.M. Ronningen, G. Bertsch, Z. Chen, C.B. Chitwood, D.J. Fields, C.K. Gelbke, W.G. Lynch, T. Nayak, J. Pochodzalla and T. Shea, Phys. Rev. Lett. 57 (1986), p 559.

SOURCES OF LIGHT PARTICLES IN PERIPHERAL COLLISIONS

P.L. Gonthier,[a] M.T. Vonk,[a] D.A. Cebra, W.K. Wilson, S. Howden, A. Nadasen,
A. Vander Molen, J.S. Winfield, and G.D. Westfall

Extensive studies[1 – 23] of correlations between light particles and projectile-like fragments in heavy ion reactions indicate that a significant yield of projectile-like fragments is accompanied by the production of light particles focused in the beam direction with velocities approaching the velocity of the beam. The emission of light particles in such peripheral collisions has been associated with various production mechanisms such as the formation of hot spots,[1, 2] Fermi jets,[8] piston effect,[9] quasi-free knockout,[10] and projectile breakup.[11, 12] In such mechanisms emission is expected to take place during the early stages of the collision, thereby providing a probe of the reaction mechanism that yields information on the dissipation of the energy during the collision. However, the projectile and target nuclei can be excited to particle unbound states that are long lived. Decay of such states leads to sequential processes. Sequential emission is the decay of statistically equilibrated projectile-like fragments (PLF's), defined here as fragments with $Z_{PLF} \approx Z_{projectile}$, and target-like fragments (TLF's), defined here as fragments with $Z_{TLF} \approx Z_{target}$, that have been fully accelerated by the Coulomb field of the two interacting nuclei. Several studies[2 – 6, 13, 21 – 23] have pointed out that the majority of the coincidence yield can be accounted for in terms of sequential decay of projectile-like and target-like fragments. As the bombarding energy increases, other nonsequential processes begin to compete in the production of light particles. The experimental challenge is to identify and separate these short and long decay processes in order to study the reaction mechanism.

The ^{16}O+Ni system and the similar system ^{16}O+Ti have been extensively studied.[1 – 6] Coincidence correlations of α particles and carbon ions have suggested the presence of two nonsequential decay processes.[2, 4 – 6] The first component consists of α particles focused in the beam direction, having velocities similar to that of the beam and with an enhanced yield on the opposite side of the beam from the detected carbon ions. This component has been referred to as the fast or beam velocity component. The second component is characterized by α particles with velocities intermediate between the beam velocity and the velocity of the center of mass. The intermediate component has a maximum yield on the opposite side of the beam from the remnants of the projectile and in the general direction of the recoiling target nucleus. The energy spectra of α particles from the intermediate component are harder than expected from the equilibrated emission of the target nucleus as observed at backward angles. However, the spectra suggest a Coulomb barrier similar to that of between the α particle and the target nucleus (TLF's).[5]

In this report we report some preliminary results of an experiment designed to separate and better identify these two production sources of α particles in the peripheral collisions of 35 MeV/nucleon ^{16}O with ^{nat}Ni. We find conclusive evidence that the fast component arises from the breakup of the projectile. Since this component cannot be accounted for by a sequential decay model, the time scale for the emission of these fast particles must be of the order of the collision time. The source of the second intermediate component of α particles, also emitted nonsequentially, is identified to be the target nucleus.

We performed the experiment in the Michigan State University (MSU) 4π Array,[24] using a beam of 35 MeV/nucleon ^{16}O ions accelerated by the K500 cyclotron at the National Superconducting Cyclotron Laboratory to irradiate a nickel foil having a nominal thickness of 2.26 mg/cm^2. Light charged particles and PLF's were detected in the forward array consisting of 45 fast/slow plastic scintillators covering an angular range between 7 and 18° with respect to the beam direction. Using in conjunction with the forward array, the MSU 4π array, consisting of fast/slow plastic scintillators, detected hydrogen and helium isotopes. The fast plastic ΔE scintillators had thicknesses of 1.6 mm and 3.2 mm in the forward array and the MSU 4π array, respectively. The forward array detectors had energy thresholds of 46 MeV and 260 MeV for α particles and carbon ions, respectively. The MSU 4π array had an α particle energy threshold of 70 MeV.

In this paper, we focus on results of particle-particle correlations measured in the forward array using the 35 MeV/nucleon ^{16}O projectiles. We refer to angles of the particle detectors on the same side of the beam as the detected PLF's with a positive sign and on the opposite side with a negative sign. The angles in this paper are given in spherical coordinates in the laboratory frame with the beam axis being the z-axis.

In Fig. 1a and 1b for multiplicity=2 events in the forward array, we present energy-energy correlations of α particles detected at the indicated angles in coincidence with carbon ions observed at +10°. As we have seen before,[5, 6] we find the signature for sequential emission observed best on the same side (Fig. 1a) of the beam as the detected carbon ions. This signature is revealed by the pattern of two high intensity regions with a pronounced valley in between them. On the opposite side of the beam in Fig. 1b, the data show only one broad pattern consisting of α particles with an average velocity of 90% of the

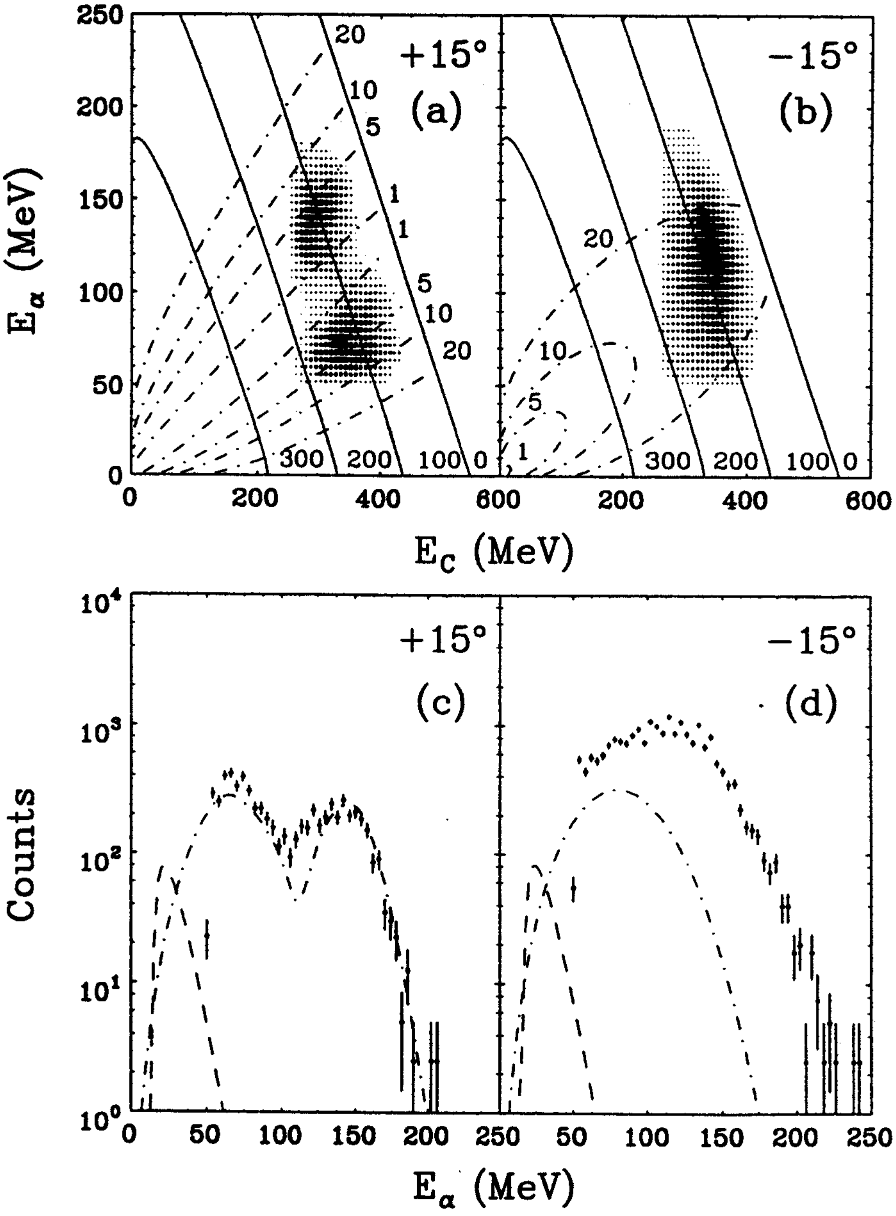

Figure 1: Density plots (Figs. 1a and 1b), with the intensity varying linearly, for α particles at the indicated angles in coincidence with carbon at $\theta_C = +10°$. The data have been smoothed using a two dimensional Gaussian distribution, and gray scaled with 8x8 pixel cells. Curves represent three body kinematic calculations. The dotdash curves correspond various values of the relative energy (MeV) between ^{12}C and α particle assuming the breakup of ^{16}O into ^{12}C + α. The solid curves correspond to the total excitation energy, Q_3 (MeV). Figs. 1c and 1d show the projections onto the energy axis of the α particles with dashed, and dotdash curves representing the calculated contributions from the sequential decay of TLF's and PLF's, respectively.

beam velocity and of carbon ions with an average velocity of 80% of the beam velocity. In Fig. 1c and 1d, we show the projections of the yields onto the α particle energy axis. The two lobes of Fig. 1a are seen as two bumps in Fig. 1c. Sequential model calculations[6] are shown as dashed curves for the sequential decay of TLF's, and dotdash curves for the sequential decay of the PLF's. The high energy thresholds of the forward array prevent the observance of the sequential component from the TLF's. As a result most of the yield at $\theta_\alpha = +15°$ is produced by the sequential breakup of ^{16}O. On the opposite side of the beam, the energy spectrum, shown in Fig. 1d, is characterized by the large bump of α particles having 90% of the beam velocity. The fast component is manifested by this excess of high energy α particles. At energies lower than 100 MeV, the spectrum also indicates an excess in the yield of α particles that cannot be accounted for in terms of the sequential emission from PLF's and TLF's. This excess at intermediate energies reflects the presence of the intermediate component of nonsequentially emitted α particles.[5]

In order to understand better the binary nature of breakup of the projectile, we examine the correlation of atomic numbers from multiplicity=2 events. Fig. 2a and 2b presents ions of atomic number Z_2 detected between $\theta_{Z_2} = \pm(7° \rightarrow 18°)$ on the same side (Fig. 2a) and opposite side (Fig. 2b) of the beam from Z_1 detected at $\theta_{Z_1} = +10°$. As can be seen along the solid line of $Z_1 + Z_2 = 8$, the $^{12}C + \alpha$ channel is the most probable two-body decay mode of ^{16}O on the both sides of the beam. There may be a substantial number of events for the proton pickup channel, $Z_1 + Z_2 = 9$ (dashed line), but many fewer for the α particle pickup channel, $Z_1 + Z_2 = 10$ (dotdashed line). The distributions in this figure along the $Z_1 + Z_2$ lines suggest that most of these fragments come from the projectile breakup. Fragments whose sum of atomic numbers is less than the atomic number of the projectile may result from the multiple decay of highly excited states of the projectile.

To test the hypothesis of the multiple breakup of the projectile, we consider multiplicity=3 events in the forward detector array in which Z_1 and Z_3 are detected on the same side of the beam. We define the xz-plane by the direction of Z_1 and the beam axis, i.e. $\phi_1 = 0°$. For particles with Z_2 detected on the opposite side of the beam from Z_1 we have selected ϕ_2 to be between 160 and 200°. Correlations between the atomic numbers of Z_1 and Z_2 on the opposite side of the beam each other are shown in Fig. 3 with the third fragment, Z_3, indicated in the figure. Since the distribution of products is limited by the solid line of $Z_1 + Z_2 + Z_3 = 8$ as in the case of multiplicity=2 events, the majority of the yield can be understood in terms of the multiple decay of the excited projectile. Such correlations of atomic numbers of products

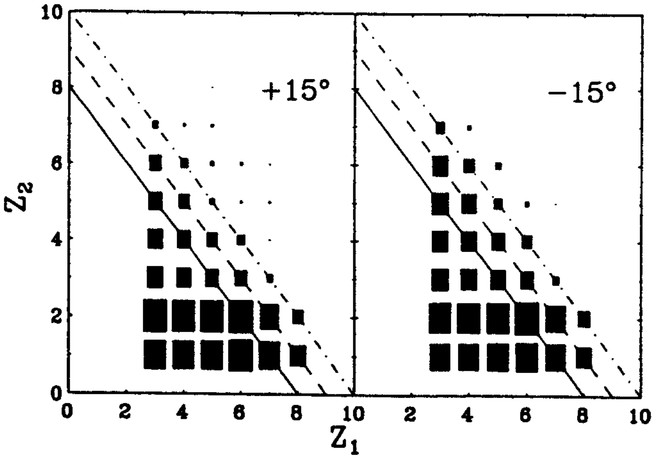

Figure 2: Coincidences between ions of atomic number Z_2 observed on the opposite side of the beam from the detected Z_1. Solid, dashed and dotted lines indicate events in which the sum of $Z_1 + Z_2$ is equal to the atomic number of the projectile, Z_{PRO}, is equal to $Z_{PRO} + 1$ and is equal to $Z_{PRO} + 2$, respectively. The intensity scale reflects the logarithm of the counts.

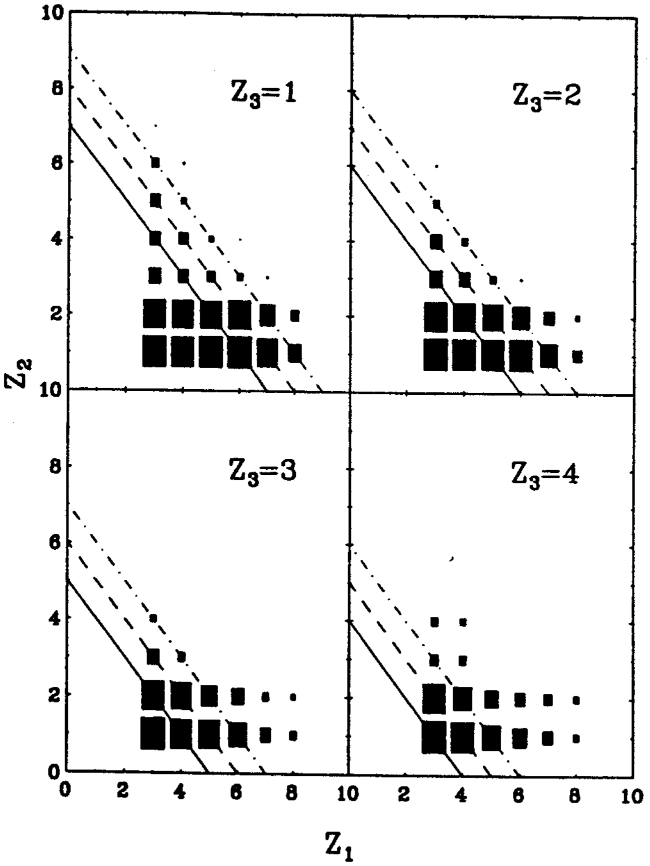

Figure 3: Triple coincidences among ions of atomic number Z_2 and Z_3 observed on the opposite side of the beam from the detected Z_1. Solid, dashed and dotted lines indicate events in which the sum of $Z_1 + Z_2 + Z_3$ is equal to the atomic number of the projectile, Z_{PRO}, is equal to $Z_{PRO} + 1$ and is equal to $Z_{PRO} + 2$, respectively. The intensity scale reflects the logarithm of the counts.

observed on the opposite sides of the beam suggest that most of the light particles emitted on the opposite side of the beam from the observed PLF's may indeed have their origin in the projectile.

In order to identify clearly the source of the fast component of α particles shown in Figs. 1b and 1d, we reconstruct the projectile by detecting an α particle in the vicinity of a ^{12}C on the same side of the beam. From Figs. 1a and 1c, we can see that the majority of the $\alpha-^{12}$C yield at $\theta_\alpha = +15°$ results from the breakup of ^{16}O. With the large energy thresholds, the contribution from the decay of TLF's as seen by the forward array is of the order of a few percent. In coincidence with the reconstructed projectile we select multiplicity=3 events where a second α particle appears on the opposite side of the beam from the detected ^{12}C. We represent in Fig. 4a by open circles, with a dashed curve to guide the eye, the energy spectrum of the second α particle on the opposite side of the beam. In order to compare the shape of this spectrum with that of multiplicity=2 events, the energy spectrum of α particles, shown previously in Fig. 1d, is presented in Fig. 4a as a histogram. As mentioned above, the fast component is manifested by the presence of the high energy bump in the histograms in Fig. 4. Since in the case of $\mathrm{C} - \alpha - \alpha$ events the projectile has been reconstructed, these α particles on the opposite side of the beam from the reconstructed projectile can only come from the target nucleus. The absence of the high energy bump in the α particle energy spectrum of $\mathrm{C} - \alpha - \alpha$–multiplicity=3 events (open circles) indicates conclusively that the fast, beam velocity component of α particles, arises from the breakup of the projectile.

In the case of $^{12}\mathrm{C} - \mathrm{p} - \alpha$ events (solid circles in Fig. 4a), the proton may come from the projectile (proton pickup) or from the target nucleus. In either case, the α particle will come mostly from the breakup of the projectile. This α particle energy spectrum shown in Fig. 4a for the $\mathrm{C} - \mathrm{p} - \alpha$ events is very similar to the energy spectrum (histogram) from $\mathrm{C} - \alpha$–multiplicity=2 events, thus confirming that the high energy α particles come from the breakup of the projectile. In the Fig. 4b, we also present the α particle energy spectra (solid circles) for the $\mathrm{B} - \alpha - \alpha$, $\mathrm{Be} - \alpha - \alpha$, and $\mathrm{Li} - \alpha - \alpha$—multiplicity=3 events. These triple coincidence energy spectra are compared to the double coincidence energy spectra for α particles in coincidence with B, Be, and Li ions (histograms). The $\mathrm{B} - \alpha - \alpha$ events select the proton pickup channel, whereas, the $\mathrm{Be} - \alpha - \alpha$ and $\mathrm{Li} - \alpha - \alpha$ events result from the direct, multiple decay of the projectile without the necessity of picking up nucleons from the target. These triple coincidence α particle energy spectra have the same shape as the spectra for the multiplicity=2 events. The presence of the fast

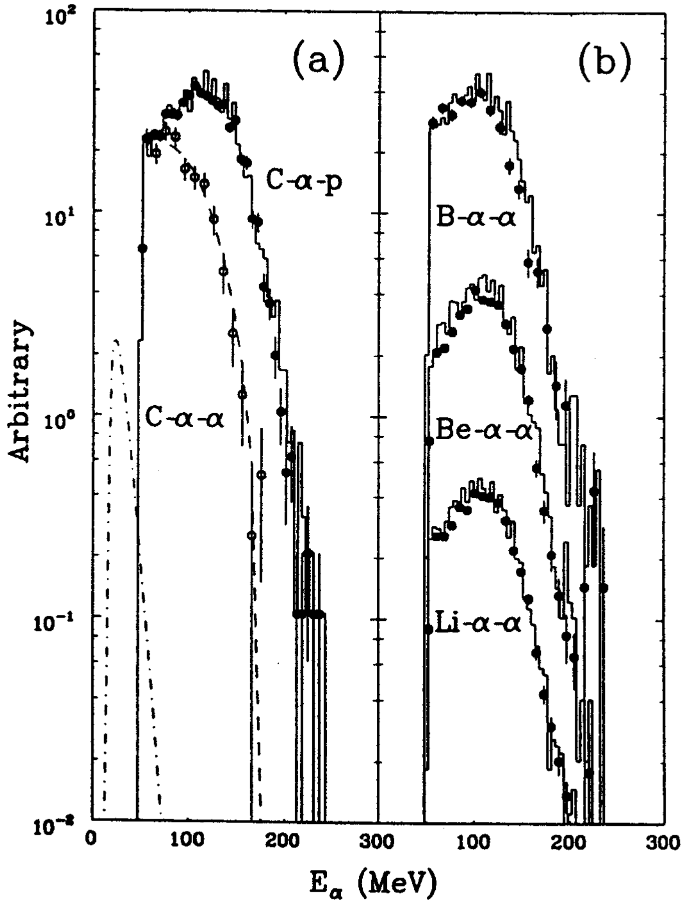

Figure 4: Energy spectrum of α particles (histogram in Figs. 4a) in coincidence with carbon ions detected on the opposite side of the beam (double coincidences). Open circles with the dashed curve to guide the eye (Fig. 4a) represent the energy spectrum of α particles detected on the opposite side of the beam from the reconstructed ^{16}O (triple coincidences). Solid circles in Fig. 4a represent $C - p - \alpha$ triple coincidence events. Dotdash curve represents the calculated contribution from the sequential decay of TLF's. Similarly, data are shown as solid circles in Fig. 4b for $B - \alpha - \alpha$, $Be - \alpha - \alpha$, and $Li - \alpha - \alpha$ triple coincidences. Energy spectra of α particles (histograms in Figs. 4b) in coincidence (double) with B, Be, and Li ions detected on the opposite side of the beam.

component in the these triple coincidence energy spectra strongly suggests that the projectile undergoes multiple α particle decay leading to the production of energetic light particles. These studies provide very conclusive evidence that the projectile is the source of the fast, beam velocity component focused on the opposite side of the beam from the detected PLF's.

The model calculation describes very well the sequential decay characteristics reflected by the shape and magnitude of the energy spectrum of α particles observed on the same side of the beam as the detected carbon ions, shown above in Fig. 1c. At these coincidence angle pairs where sequential decay processes are separated most clearly, we fix the parameters in the model associated with the excitation energy distribution and energy and angular distributions of the primary ^{16}O prior to decay. With this set of parameters that best describe the data on the same side of the beam, we are unable to describe the Fig. 1d, of α particles detected on the opposite side of the beam. Even though the fast, beam velocity component has its origin in the projectile, such α particles do not come from sequential emission processes and so, must be emitted on a time scale shorter than the time scale for sequential emission.

The dotdashed curve in Fig. 4a represents the calculated energy spectrum of α particles emitted sequentially by TLF's in coincidence with carbon ions. These calculations are based on the α particle energy spectra observed at backward angles.[5] For $C - \alpha - \alpha$ events, the energy spectrum of α particles, that must come from the TLF's, are much harder than the expected spectrum for α particles emitted sequentially by the TLF's. We draw the conclusion that the TLF's are definitely the source of the intermediate component of α particles. Since for these events the projectile is reconstructed, and, therefore, cannot be the source. Because the intermediate component of α particles cannot be accounted for in terms of sequential decay processes, it must be produced during the early stages of the collision.

A concept that might explain the data is a quasi-free scattering or knockout process in which the projectile scatters off an α particle cluster that is preformed or formed during the collision on the surface of the target nucleus. During this process the α particle is removed from the target, and the projectile is excited to an α particle unbound state. The Fermi momentum distribution of the α particle cluster in the target nucleus smears the correlation between it and the reconstructed projectile on the opposite side of the beam.

In conclusion, we find that that triple coincidence correlations between the reconstructed projectile and an α particle detected on the opposite side of the beam from the detected ^{12}C conclusively reveal that the fast, beam velocity component of α particles previously observed in coincidence with projectile-like fragments arises from the breakup of the projectile. In addition, the correlations clearly show that the target nucleus is the origin of the intermediate component of α particles. Both of these components are produced by mechanisms leading to the emission of α particles during the early stages of the collision.

a. Hope College, Holland, MI

References

1. H. Ho, R. Albrecht, W. Dünnweber, G. Graw, S.G. Steadman, J.P. Wurm, D. Disdier, V. Rauch, and F. Scheibling, Z. Phys. A283 (1977), p 235.

2. H. Ho, P. Gonthier, M.N. Namboodiri, J.B. Natowitz, L. Adler, S. Simon, K. Hagel, R. Terry, and A.Khodai. Phys. Lett. 96B (1980), p 51.
3. H.Ho, P.L. Gonthier, G.-Y. Fan, W. Kühn, A. Pfoh, L. Schad, R. Wolski, J.P. Wurm, J.C. Adloff, D. Disdier, A. Kamili, V. Rauch, G. Rudolf, F. Scheibling, and A. Strazzeri, Phys. Rev. C27 (1983), p 584.
4. P.L. Gonthier, H. Ho, N.M. Namboodiri, J.B. Natowitz, L. Adler, S. Simon, K. Hagel, S. Kniffen, and A. Khodai, Nucl. Phys. A411 (1983), p 289.
5. P.L. Gonthier, B. Bouma, P. Harper, R. Ramaker, D.A. Cebra, Z.M. Koenig, D. Fox, and G.D. Westfall, Phys. Rev. C35 (1987), p 1946.
6. P.L. Gonthier, P. Harper, B. Bouma, R. Ramaker, D.A. Cebra, Z.M. Koenig, D. Fox, and G.D. Westfall, Phys. Rev. C41 (1990), p 2635.
7. P.A. Gottschalk and M. Weström, Nucl. Phys. A314, 232 (1979), p 232.
8. J.P. Bondorf, J.N. De, G. Fai, A.O.T. Karvinen, B. Jakobsson, and J. Randrup, Nucl. Phys. A333 (1980), p 285, M.C. Robel, Ph. D. thesis, Lawrence Berkeley Laboratory Report LBL-8181, (1979).
9. D.H.E. Gross and J. Wilczynski, Phys. Lett. 67B (1977), p 1.
10. R.K. Bhowmik, E.C Pollacco, N.E. Sanderson, J.B.A. England, and G.C Morrison, Phys. Rev. Lett. 43 (1979), p 619.
11. R. Billerey, C. Cerruti, A. Chevarier, N. Chevarier, B. Cheynis, and A. Demeyer, Z. Phys. A292 (1979), p 293.
12. A. Gamp, J.C. Jacmart, N. Poffe, H. Doubre, J.C. Roynette, and J. Wilczynski, Phys. Lett. 74B (1978), p 215.
13. J. van Driel, S. Gonggrijp, R.V.F. Janssens, R.H. Siemssen, K. Siwek-Wilczynska, and J. Wilczynski, Phys. Lett. 98B (1981), p 351.
14. W.D. Rae, A.J. Cole, A. Dacal, R. Legrain, B.G. Harvey, J. Mahoney, M.J. Murphy, R.G. Stokstad, and I. Tserruya, Phys. Lett. 105B (1981), p 417.
15. W. Terlau, M. Bürgel, A. Budzanowski, H. Fuchs, H. Homeyer, G. Röschert, J. Uckert, and R. Vogel, Z. Phys. A330 (1988), p 303.
16. M.B. Tsang, W.G. Lynch, R.J. Puigh, R. Vandenbosch, and A. G. Seamster, Phys. Rev. C23 (1981), p 1560.
17. R. K. Bhowmik, J. van Driel, R.H. Siemssen, G.J. Balster, P.B. Goldhoorn, S. Gonggrijp, Y. Iwasaki, R.V.F. Janssens, H. Sakai, K. Siwek-Wilczynska, W.A. Sterrenburg, and J. Wilczynski, Nucl. Phys. A390 (1982), p 117.
18. H. Homeyer, M. Bürgel, M. Clover, Ch. Egelhaaf, H. Fuchs, A. Gamp, D. Kovar, and W. Rauch, Phys. Rev. C26 (1982), p 1335.
19. E. Takada, T. Shimoda, N. Takahashi, T. Yamaya, K. Nagatani, T. Udagawa, and T. Tamura, Phys. Rev. C23 (1981), p 772.
20. T. Fukuda, M. Ishihara, M. Tanaka, I. Miura, H. Ogata, and H. Kamitsubo, Phys. Rev. C25 (1982), p 2464.
21. G.R. Young, R.L. Ferguson, A. Gavron, D.C. Hensley, Felix E. Obenshain, F. Plasil, A.H. Snell, M.P. Webb, C.F. Maguire, and G.A. Petitt, Phys. Rev. Lett. 45 (1980), p 1389.
22. H. Gemmeke, P. Netter, Ax. Richter, L. Lassen, S. Lewandowski, W. Lücking, and R. Schreck, Phys. Lett. 97B (1980), p 213.
23. M. Bini, C.K. Gelbke, D.K. Scott, T.J.M. Symons, P. Doll, D.L. Hendrie, J.L. Laville, J. Mahoney, M.C. Mermaz, C. Olmer, K. Van Bibber, and H.H. Wieman, Phys. Rev. C22 (1980), p 1945.
24. G.D. Westfall, J.E. Yurkon, J. Van der Plicht, Z.M. Koenig, B.V. Jacak, R. Fox, G.M. Crawley, M.R. Maier, and B.E. Hasselquist, Nucl. Inst. and Meth. A238 (1985), p 347.

INTENSITY-INTERFEROMETRIC TEST OF NUCLEAR COLLISION GEOMETRIES OBTAINED FROM THE BOLTZMANN-UEHLING-UHLENBECK EQUATION

W.G. Gong, W. Bauer, C.K. Gelbke, N. Carlin,[a] R.T. deSouza, Y.D. Kim, W.G. Lynch, T. Murakami,[b] G. Poggi,[c] D.P. Sanderson, M.B. Tsang, H.M. Xu, S. Pratt,[d] D.E. Fields,[e] K. Kwiatkowski,[e] R. Płaneta,[f] V.E. Viola, Jr.,[e] and S.J. Yennello[e]

Microscopic models of intermediate energy nucleus-nucleus collisions have been successfully based on the semiclassical Boltzmann-Uehling-Uhlenbeck (BUU) equation[1] which describes the temporal evolution of the one-body density under the influence of the nuclear mean field and individual nucleon-nucleon collisions. In this report, we present the first quantitative test of the space-time geometry predicted by solutions of the BUU equation by using the technique of two-proton intensity interferometry[2,3] which utilizes the space-time sensitivity of the two-proton correlation function at small relative momenta. For this purpose, we have measured two-proton correlation functions with high statistical accuracy for the relatively light projectile-target combination, $^{14}N + ^{27}Al$, at E/A=75 MeV.[4,5] For such a light system, numerical calculations can be performed with good accuracy and modest amounts of CPU time.

The experiment was performed with a 75MeV/nucleon ^{14}N beam from the NSCL K1200 cyclotron on an ^{27}Al target of 15mg/cm^2 areal density. Protons were detected with two ΔE-E detector arrays consisting of 300-400μm thick silicon ΔE-detectors and 10cm long CsI(Tl) or NaI(Tl) E-detectors. An array consisting of 37 Si-CsI(Tl) [7] telescopes was centered at the polar and azimuthal angles of $\Theta = 25^0$ and $\Phi = 0^0$; each of its detectors had a solid angle of $\Delta\Omega = 0.37msr$ and a nearest neighbor spacing of $\Delta\theta = 2.6^0$. Another array consisting of 13 Si-NaI(Tl) telescopes was centered at $\Theta = 25^0$ and $\Phi = 90^0$; each of its detectors had a solid angle of $\Delta\Omega = 0.5msr$ and a nearest neighbor spacing of $\Delta\theta = 4.4^0$. Coincidence and downscaled singles data were taken simultaneously. Energy calibrations are accurate to better than 2%. Typical detector energy resolutions were of the order of 2% and 1% for protons of 40 MeV and 100 MeV, respectively. All data were corrected for random coincidences and had a software energy threshold of 10 MeV.

The experimental two-proton correlation function, R(q), is defined in terms of the coincidence yield, $Y_{12}(\mathbf{p}_1, \mathbf{p}_2)$, and the single proton yields, $Y_1(\mathbf{p}_1)$ and $Y_2(\mathbf{p}_2)$:

$$\sum Y_{12}(\mathbf{p}_1, \mathbf{p}_2) = C_{12}[1 + R(q)] \sum Y_1(\mathbf{p}_1) Y_2(\mathbf{p}_2) \tag{1}$$

Here, $\mathbf{p}_1$ and $\mathbf{p}_2$, are the laboratory momenta of the two protons, and $q = \frac{1}{2}|\mathbf{p}_2 - \mathbf{p}_1|$ is the relative

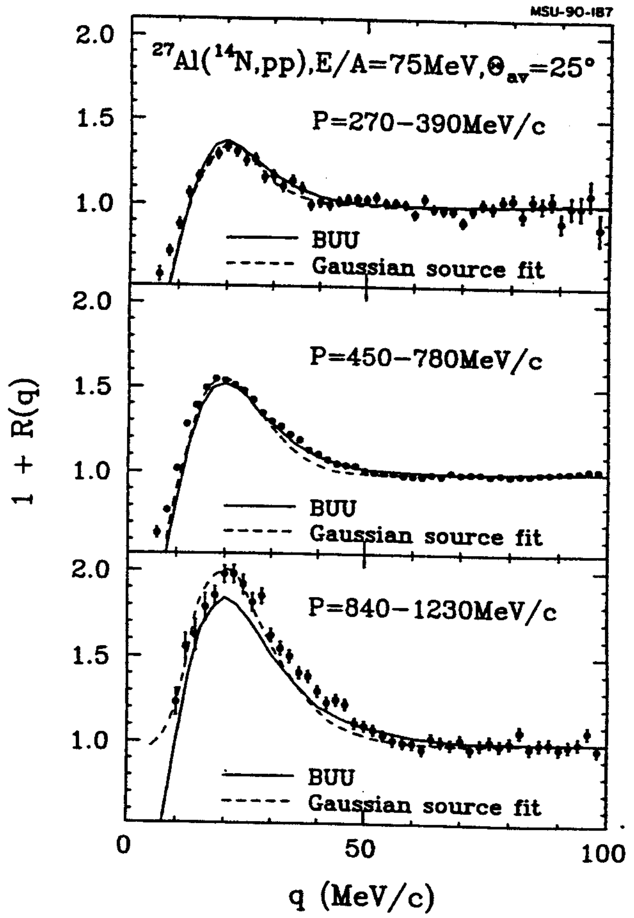

Figure 1: Two-proton correlation functions measured for the reaction $^{14}N + ^{27}Al$ at E/A=75 MeV. The gates placed on the total momenta, P, of the coincident proton pairs are indicated. The dashed curves represent calculations for Gaussian sources of negligible lifetime, assuming the momentum dependence of the radius parameter, $r_0(P)$, shown by the solid points in Fig.2. The solid curves correspond to solutions of the BUU equation using the stiff equation of state, Eq.7.

momentum of the proton pair. For each experimental gating condition, the sums on both sides of Eq.1 are extended over all energy and detector combinations corresponding to specific relative momentum bins. The normalization constant, C_{12}, is determined from the requirement R(q)=0 at large q.

Our theoretical analysis is based upon the expression:[4,5]

$$1 + R(\mathbf{P},\mathbf{q}) = \int d^3\mathbf{r}\, F_{\mathbf{P}}(\mathbf{r})|\phi(\mathbf{q},\mathbf{r})|^2 \tag{2}$$

where $\mathbf{P} = \mathbf{p}_1 + \mathbf{p}_2$ is the total momentum of the proton pair, $\phi(\mathbf{q},\mathbf{r})$ is the relative two-proton wave function, and $F_{\mathbf{P}}(\mathbf{r})$ is defined by:

$$F_{\mathbf{P}}(\mathbf{r}) = \frac{\int d^3\mathbf{R}\, f(\frac{1}{2}\mathbf{P},\mathbf{R}+\frac{1}{2}\mathbf{r},t_>)f(\frac{1}{2}\mathbf{P},\mathbf{R}-\frac{1}{2}\mathbf{r},t_>)}{|\int d^3\mathbf{R}\, f(\frac{1}{2}\mathbf{P},\mathbf{R},t_>)|^2}, \tag{3}$$

Here, the Wigner function, $f(\mathbf{p},\mathbf{r},t_>)$, is the phase-space distribution of protons of momentum p at position

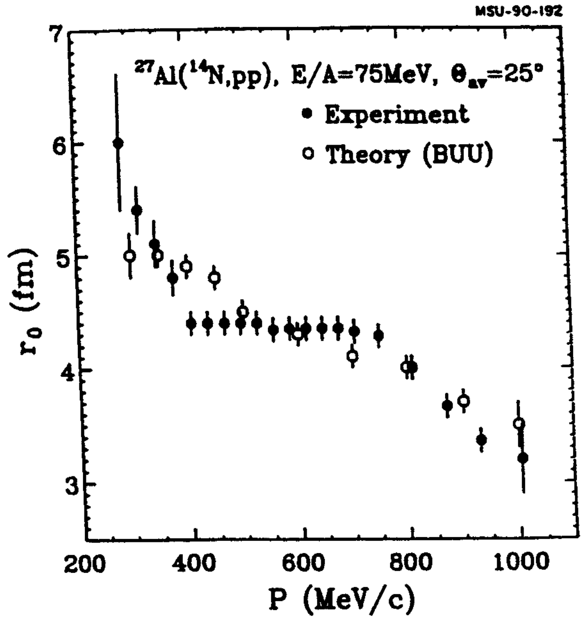

Figure 2: Radius parameters, $r_0(P)$, for Gaussian sources of negligible lifetime extracted from two-proton correlation functions gated by different total momenta, P. Solid and open points represent experimental and theoretical correlation function, respectively.

r at some time $t_>$ after the emission process. $f(\mathbf{p},\mathbf{r},t_>)$ can be related to the emission function $g(\mathbf{p},\mathbf{r},t)$ by:

$$f(\mathbf{p},\mathbf{r},t_>) = \int_{-\infty}^{t_>} dt\, g(\mathbf{p},\mathbf{r}-\mathbf{p}(t_> - t)/m, t). \tag{4}$$

Fig.1 shows measured two-proton correlation functions for representative ranges of the total momentum, P, of the proton pairs. In order to describe the dependence on P in terms of a simple variable, we have constructed experimental correlation functions for a number of narrow gates on P. Each such correlation function was characterized in terms of a simple Gaussian source of negligible lifetime,

$$g(\mathbf{P}/2,\mathbf{r},t) = \rho_0 \cdot exp[-r^2/r_0(P)^2]\delta(t - t_0) \tag{5}$$

The extracted source parameters, $r_0(P)$, are shown by the solid points in Fig.2 The error bars indicate estimated systematic uncertainties. The dashed curves in Fig.1 show examples of fits with Eq.5 which are used to extract the momentum dependence of $r_0(P)$ shown in Fig.2. In these calculations, appropriate averages over total momentum and the calculated resolution of the hodoscope were taken into account.

In order to compare our results with microscopic dynamical calculations, we have calculated microscopic Wigner functions by solving the BUU transport equation:[1,6]

$$\partial_t f(\mathbf{p},\mathbf{r},t) + \frac{\mathbf{p}}{m} \cdot \nabla_{\mathbf{r}} f(\mathbf{p},\mathbf{r},t) - \nabla_{\mathbf{r}} U(\mathbf{r}) \cdot \nabla_{\mathbf{p}} f(\mathbf{p},\mathbf{r},t) = \frac{1}{2\pi^3 m^2} \cdot$$
$$\int d^3q'_1 d^3q_2 d^3q'_2 \delta[\frac{1}{2m}(p^2 + q_2^2 - q'^2_1 - q'^2_2)]\delta^3(\mathbf{p} + \mathbf{q_2} - \mathbf{q'_1} - \mathbf{q'_2})\frac{d\sigma}{d\Omega} \cdot$$

$$\{\hat{f}(\mathbf{q'}_1,\mathbf{r},t)\hat{f}(\mathbf{q'}_2,\mathbf{r},t)[1-\hat{f}(\mathbf{p},\mathbf{r},t)][1-\hat{f}(\mathbf{q}_2,\mathbf{r},t)]$$
$$-\hat{f}(\mathbf{p},\mathbf{r},t)\hat{f}(\mathbf{q}_2,\mathbf{r},t)[1-\hat{f}(\mathbf{q'}_1,\mathbf{r},t)][1-\hat{f}(\mathbf{q'}_2,\mathbf{r},t)]\}. \tag{6}$$

where, $\hat{f}$(p,r,t) is the phase space density. The in-medium nucleon-nucleon scattering cross section, $d\sigma/d\Omega$, was assumed to be proportional to the experimentally known (energy-dependent) cross section for free nucleons, $d\sigma_{nn}/d\Omega$. The mean field, U(r), was approximated by density-dependent, simplified local Skyrme interactions:

$$U(\rho) = -124(\rho/\rho_0) + 70.5(\rho/\rho_0)^2, \tag{7}$$
$$U(\rho) = -356(\rho/\rho_0) + 303(\rho/\rho_0)^{7/6}. \tag{8}$$

Here, ρ_0 denotes the equilibrium density of normal nuclear matter. Equations 7 and 8 represent a stiff and a soft equation of state with compressibility coefficients κ= 380 MeV and 200 MeV, respectively. The left hand side of the Eq.6 is the Vlasov term describing the interaction of the nucleons with the mean field; the right-hand side is the collision integral which includes a semiclassical Pauli-blocking factor. This equation was solved by using test particle method.[1,6] By explicitly storing $\hat{f}$(p,r,t) on a six-dimensional lattice in every time-step we were able to greatly speed up the computer program without relaxing the accuracy of the treatment of the Pauli-exclusion principle.[6] Nucleon emission was calculated for a time interval of Δt_e=140 fm/c following initial contact of the colliding nuclei. Nucleons were considered as emitted when the surrounding density fell below $\rho_e = \rho_0/8$ and when subsequent interaction with the mean field did not cause recapture into regions of higher density. At present, these parameters must be treated as unknown model parameters which may introduce uncertainties of the order of 5-10% into the magnitude of the predicted correlation functions. For the calculation of a correlation function, we generated phase space points from a total of 5250 events with impact parameters distributed according to their geometrical weights; appropriate averages over impact parameter, orientation of the reaction plane, and momenta of the the outgoing particles were taken into account.

Correlation functions calculated from Wigner functions predicted by the BUU equation are shown by the solid lines in Fig.1. For these calculations, we used the stiff equation of state, Eq.7, and the free nucleon-nucleon scattering cross section, $d\sigma/d\Omega = d\sigma_{nn}/d\Omega$. In order to facilitate a more detailed comparison with the experimental data, the predicted correlation functions were characterized in terms of equivalent Gaussian sources, Eq.5, following the procedure outlined above. The corresponding equivalent radius parameters, $r_0(P)$, are shown by the open points in Fig.2. The errors represent estimates for the

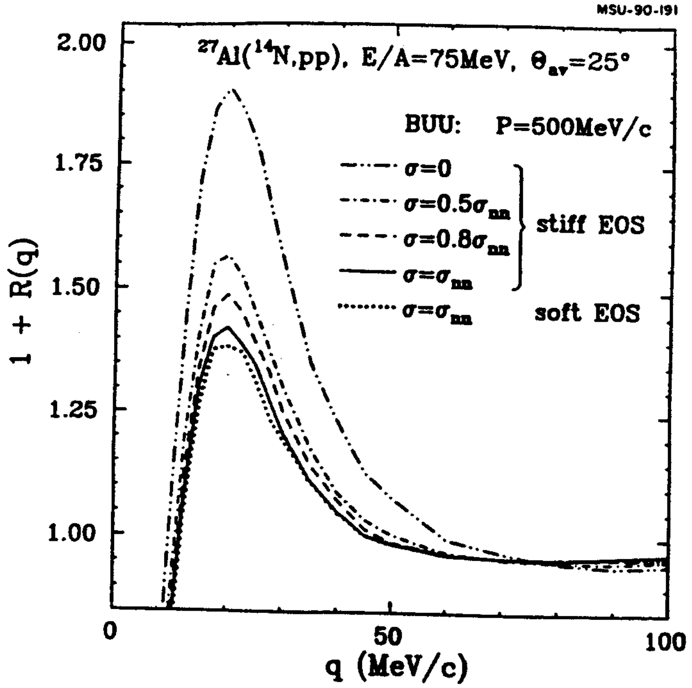

Figure 3: Sensitivity of two-proton correlation function at intermediate momentum to the nuclear equation of state and the in-medium nucleon-nucleon cross section.

numerical accuracy of our calculations. The predicted correlation functions are in good agreement with the data indicating that the BUU equation gives a good overall description of the average space-time evolution of the reaction.

We have also explored the sensitivity of the calculated correlation functions to the nuclear equation of state and the magnitude of the in-medium nucleon-nucleon cross section. Fig.3 shows correlation functions predicted for intermediate momentum proton pairs, P=500 MeV/c. The solid and dotted curves show correlation functions predicted for the stiff and soft equations of state, using $d\sigma/d\Omega = d\sigma_{nn}/d\Omega$. The two calculations are very similar, indicating little sensitivity to the nuclear equation of state. This weak sensitivity to the stiffness of the equation of state may be related to the small size of projectile and target investigated here. Calculations for heavier systems and different incident energies should be pursued in future. The solid, dashed, dot-dashed, and dot-dot-dashed curves represent calculations with the stiff equation of state performed assuming that the in-medium nucleon-nucleon cross-section is equal to 1.0, 0.8, 0.5 and 0.0 times the free nucleon-nucleon cross section. The predicted correlation functions become more pronounced for decreasing values of $d\sigma/d\Omega$, indicating that increased nucleon-nucleon scattering leads to slower emission time scales. For intermediate total momenta of the proton pairs, P=500 MeV, the calculated correlation functions are rather sensitive to the magnitude of the in-medium nucleon-nucleon cross section. For the emission of very energetic particles, $P > 800$ MeV/c, this sensitivity is reduced. The measured correlation functions are rather well reproduced by calculations using free nucleon-nucleon cross sections, see Figs.1 and 2 the agreement is significantly worse when in-medium cross sections are used which are smaller than one-half of the free nucleon-nucleon cross section.

In summary, we have investigated two-proton correlation functions for $^{14}N + ^{27}Al$ collisions at E/A=75 MeV. Microscopic calculations based upon solutions of the BUU transport equation are in good agreement with the measured correlation functions, indicating that the theory predicts reasonable space-time geometries for nonequilibrium light particle emission. The predicted correlation functions are rather insensitive to the stiffness of the equation of state, but exhibit considerable sensitivity to the magnitude of the in-medium nucleon-nucleon cross section. The measured correlation functions are rather well reproduced by calculations in which the in-medium cross section is approximated by the energy-dependent free nucleon-nucleon cross section.

a. Instituto de Fisica, Universidade de São Paulo, CP20516, CEP 01498, São Paulo, Brazil.
b. Dept. of Physics, Kyoto University, Kyoto 606, Japan.
c. Dipartimento di Fisica dell'Universitã and INFN, Largo Enrico Fermi 2, 50125 Firenze, Italy.
d. Dept. of Physics, Univ. of Wisconsin, Madison, WI53706, USA.
e. Indiana University Cyclotron Facility, Indiana Univ. Bloomington, IN47405, USA.
f. Institute of Nuclear Physics, Jagellonian University, Krakow, Poland.

References

1. G.F. Bertsch and S. Das Gupta, Phys. Rep. 160, (1988), p189.
2. S.E. Koonin, Phys. Lett. 70B, (1977), p 43.
3. D.H. Boal, C.K. Gelbke, and B.K. Jennings, Rev. Mod. Phys. 62,(1990), p 553
4. W.G. Gong, et al., Phys. Rev. Lett. 65, 2114(1990).
5. W.G. Gong, W. Bauer, C.K. Gelbke, and S. Pratt, Phys. Rev. C43,p 781.
6. A detailed account of the numerical method is given in W. Bauer, Michigan State University report MSUCL-699 (unpublished).
7. W.G. Gong et al., Nucl. Instr. and Meth. A268, (1988), p 190.

TIME SCALE FOR EMISSION OF INTERMEDIATE MASS FRAGMENTS IN ^{36}Ar+^{197}Au COLLISIONS AT E/A=35 MeV

Y.D. Kim, R.T. de Souza, D.R. Bowman, N. Carlin[a], C.K. Gelbke, W.G. Gong, W.G. Lynch, L. Phair, M.B. Tsang, F. Zhu, and S. Pratt[b]

We have applied the technique of intensity interferometry[1-3] to multifragment decays and have extracted time scales for the emission of Z=4-6 fragments in the ^{36}Ar+^{197}Au reaction at E/A=35 MeV. The experiment was performed with an ^{36}Ar beam of E/A=35 MeV, produced by the K500 cyclotron of the NSCL at Michigan State University. The areal density of the gold target was 1 mg/cm^2. Light particles and complex fragments were detected with the MSU Miniball[4] with an angular coverage of Θ_{lab}=16°-160° and solid angle of 85% of 4π. Two-fragment correlation functions were constructed from intermediate mass fragments detected in rings 2 and 3. Detectors in these rings are centered at polar angles of Θ_2=19.5° and Θ_3=27° and subtend intervals in polar and azimuthal angles of $\Delta\Theta_2$=7°, $\Delta\phi_2$=22.5° and $\Delta\Theta_3$=8°, $\Delta\phi_3$=18°, respectively.

Inclusive energy spectra of Be, B, and C fragments detected in rings 2 and 3 are shown in Fig. 1. The shapes of the energy spectra are similar to those observed in other heavy-ion induced reactions at comparable energies and are indicative of large contributions from noncompound emission mechanisms, see e.g. ref. 5. The detection of one or two intermediate mass fragments in rings 2 or 3 selected events with a most probable charged particle multiplicity of about 10 which is close to the location of the central collision peak of the inclusive multiplicity distribution.

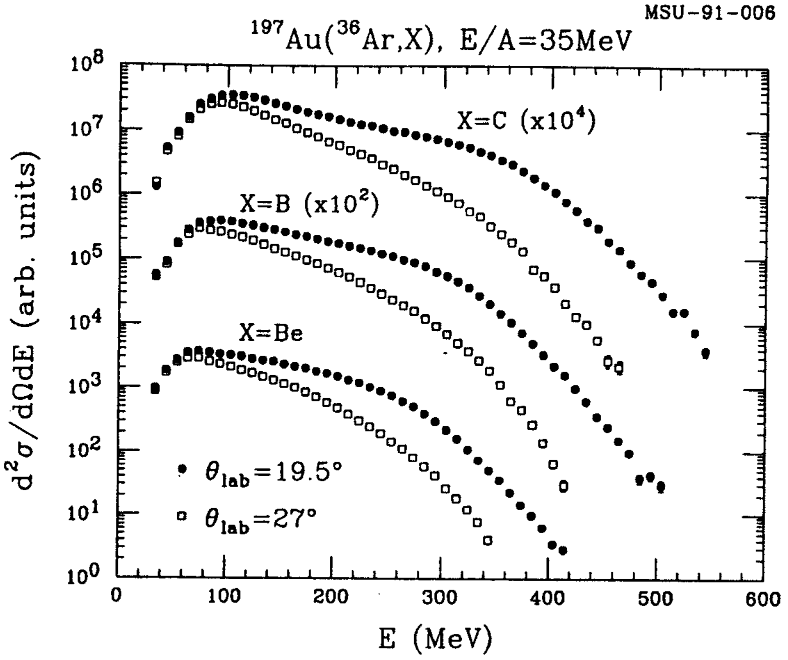

Fig. 1: Inclusive energy spectra of Be, B, and C fragments for the ^{36}Ar+^{197}Au reaction at E/A=35 MeV.

Experimental two-fragment correlation functions are shown in Fig. 2. The top, center, and bottom panels show Be-Be, B-B, and C-C correlation functions. The left panels present inclusive correlation functions and the right panels show correlation functions

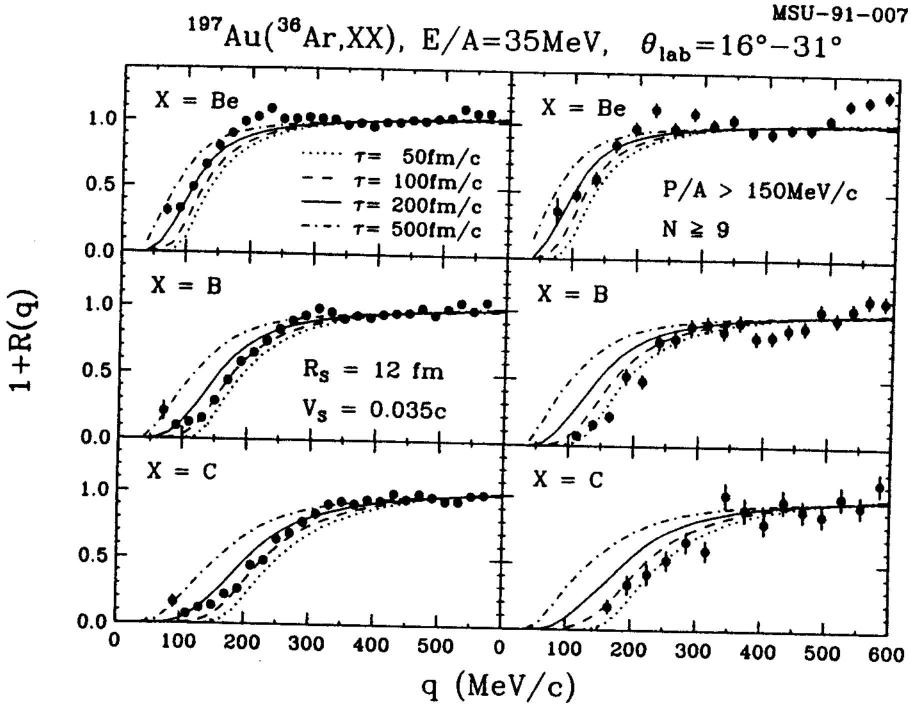

Fig. 2: Inclusive (left hand panels) and gated (right hand panels) two-fragment correlation functions at small relative momenta. The calculations are explained in the text.

gated by the requirement N≥9 and P/A>150 MeV/c, where N denotes the total number of charged particles detected in the Miniball and P/A is the total momentum per nucleon of the coincident fragment pair. All correlation functions exhibit pronounced minima at q≈0 MeV/c which can be attributed to the repulsive final-state Coulomb interaction between the emitted fragments.

The curves shown in the figure represent calculations with the formalism of ref. 3, generalized to the case of two intermediate mass fragments. Since average fragment separations are expected to be larger than the range of the nuclear force, we neglect nuclear interactions and treat the final-state Coulomb interaction between the two coincident fragments classically. In this approximation, the two-fragment correlation function can be expressed as

$$1+R(q) = \frac{\int d^3r \, F_{\vec{P}}(\vec{r}) \left[1 - \frac{2\mu Z^2 e^2}{q^2 r}\right]^{1/2}}{\int d^3r \, F_{\vec{P}}(\vec{r})}, \quad (1)$$

where, Z is the fragment charge, $\mu=\frac{1}{2}m$ is the reduced mass, and $F_{\vec{P}}(\vec{r})$ is the distribution of relative coordinates between the two particles, each emitted with momentum $\vec{p}=\frac{1}{2}\vec{P}$ (see Eqs. 23 and 24 of ref. 3). For the calculations presented in Fig. 2, $F_{\vec{P}}(\vec{r})$ was calculated by assuming the fragments to be emitted from incomplete fusion residues moving with a source velocity V_S=0.035c, a value consistent with the systematics of linear momentum transfer for reactions producing heavy reaction residues[6]. For simplicity, the emitted fragments and the heavy reaction residues were assumed to be separated by R_S=12 fm at the time of emission. The distribution of emission points on the surface of the heavy reaction residue was taken from Lambert's Law for surface emission. An exponential probability distribution of emission times was assumed, $P(t) = (1/\tau)e^{-t/\tau}$, with mean emission times τ given in the figure. The simulated energy and angular distributions of the fragments were chosen in accordance with the measured single fragment distributions.

The comparison between measured and calculated correlation functions in Fig. 2 indicates that the inclusive correlation functions are reasonably consistent with mean emission times of about $\tau \approx 100$-200 fm/c. The correlation functions gated by $N \geq 9$ and P/A>150 MeV/c appear to indicate slightly shorter emission time scales.

In our calculations, we neglect the possibility that highly excited primary fragments could undergo sequential decays by particle emission. Such decays may be expected to attenuate the minimum at $q \approx 0$ MeV/c. It is, therefore, possible that our analysis yields mean emission times which are slightly larger than those of the primary fragments[7].

The derivation of Eq. 1 is based upon the assumption that dynamical correlations and distortions in the Coulomb field of the residual nucleus can be neglected. For the present reaction, the charged particle multiplicities are sufficiently low to virtually guarantee the survival of a heavy reaction residue (which might subsequently fission). To assess the influence of the Coulomb field of the heavy reaction residue, we have performed three-body Coulomb trajectory calculations which consider the sequential emission of two carbon nuclei from the surface of a residual nucleus initially with charge number Z_S=93, mass number A_S=226, and velocity V_S=0.035c. As before, we assumed an exponential probability distribution of emission times and fragment energy distributions consistent with the measured carbon spectrum. For the emission of the second fragment, we required a minimum initial separation of 7.4 fm from the first fragment. The response of the experimental apparatus was included. In Fig. 3a, the results of these calculations (curves) are compared to the inclusive C-C correlation function (points). The three-body Coulomb trajectory calculations predict wider minima in the correlation functions than the calculations based upon Eq. 1, and the agreement with the data is slightly worse. Nevertheless, the calculations are in fair agreement with the experimental correlation functions for emission times of the order of 100-200 fm/c. In Fig. 3b, we compare calculations for τ=200 fm/c. The curve shows the calculation with Eq. 1 and the solid points show the results of the three-body trajectory calculation. The discrepancy between the two model calculations is largely caused by dynamical correlations caused by the recoil of the heavy reaction residue which

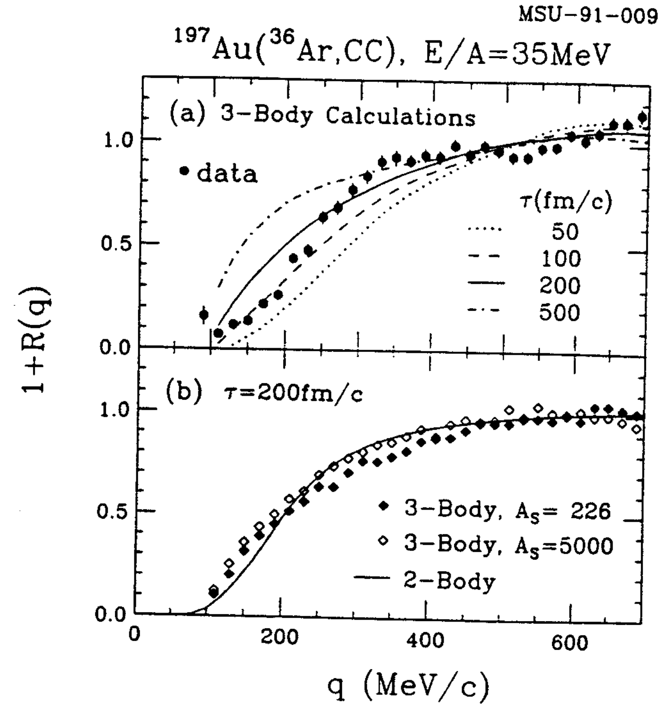

Fig. 3: Panel (a): Comparison of inclusive C-C correlation functions to three-body Coulomb trajectory calculations. Panel (b): Correlation functions calculated from Eq. 2 (curve) and from three-body trajectory calculations (points).

is included in the trajectory calculation, but not in Eq. 1. Indeed, the calculation with Eq. 1 is in rather good agreement with three-body calculations when the recoil of the heavy target residue is artificially reduced by increasing its mass to A_S=5000 while keeping its charge and radius constant (open points). These calculations suggest that the detailed shape of the predicted correlation function is influenced by the reaction dynamics and that additional insight may be gained by calculating correlation functions from more realistic reaction models.

In summary, two-fragment correlation functions for the ^{36}Ar+^{197}Au reaction indicate mean fragment emission times of the order of 100-200 fm/c. These mean emission times are shorter than those extracted previously[1,8] for reactions induced by lighter projectiles. For the present reaction, the emission times are slightly shorter than those calculated from evaporation models[9].

a. Present address: Instituto de Fisica, Universidade de Sao Paulo, C. Postal 20516, CEP 01498, Sao Paulo, Brazil

b. Department of Physics, University of Wisconsin, Madison, WI 53706, USA

References

1. R. Trockel et al., Phys. Rev. Lett. 59, 2844 (1987).
2. S.E. Koonin, Phys. Lett. 70B, 43 (1977).
3. W.G. Gong et al., Phys. Rev. C43, 781 (1991).
4. R.T. de Souza et al., Nucl. Instr. and Meth. A295, 109 (1990).
5. D.E. Fields et al., Phys. Lett. B220, 356 (1989).
6. M. Fatyga et al., Phys. Rev. Lett. 55, 1376 (1985).
7. H.W. Barz et al., Phys. Lett. B244, 161 (1990).
8. R. Bougault et al., Phys. Lett. B232, 291 (1989).
9. W.A. Friedman, Phys. Rev. Lett. 60, 2125 (1988); Phys. Rev. C40, 2055 (1989); Phys. Rev. C42, 667 (1990); and private communication.

ISOTOPE YIELD RATIOS OF FRAGMENTS FROM HEAVY-ION REACTIONS

F. Deak,[a] A. Kiss,[a] Z. Seres,[b] A. Galonsky and L. Heilbronn

In heavy-ion collisions at 84 MeV/nucleon it was found[1] that the yield ratio for three isotope pairs had an exponential dependence on N/Z. Barz et al.[2] were able to obtain the exponential behavior with a statistical multifragmentation model. They showed that the linear dependence of neutron chemical potential on N/Z, $\mu_N = \mu_{N_0} + \mu'_N(N/Z)$, gives for the isotope yield ratio the approximate dependence on N/Z

$$R \sim \exp[-(\Delta N)\mu_N/T] \sim \exp[-(\Delta N)\mu'_N(N/Z)/T], \qquad (1)$$

where T is the source temperature and ΔN is the difference in the number of neutrons of the two isotopes.

In two experiments[3,4] with a ^{14}N beam at 35 MeV/nucleon from the K500 cyclotron yields were measured for isotopes of Li, Be, B, and C from targets of C, Ni, Ag, and Ho. In all cases the quasi-elastic component was separated out, and only the deep-inelastic part was used for determining yield ratios.

The yield ratios for each element are plotted in Fig. 1 against N/Z, where N and Z are the neutron and proton numbers for the combined system, projectile-plus-target. The left part of the

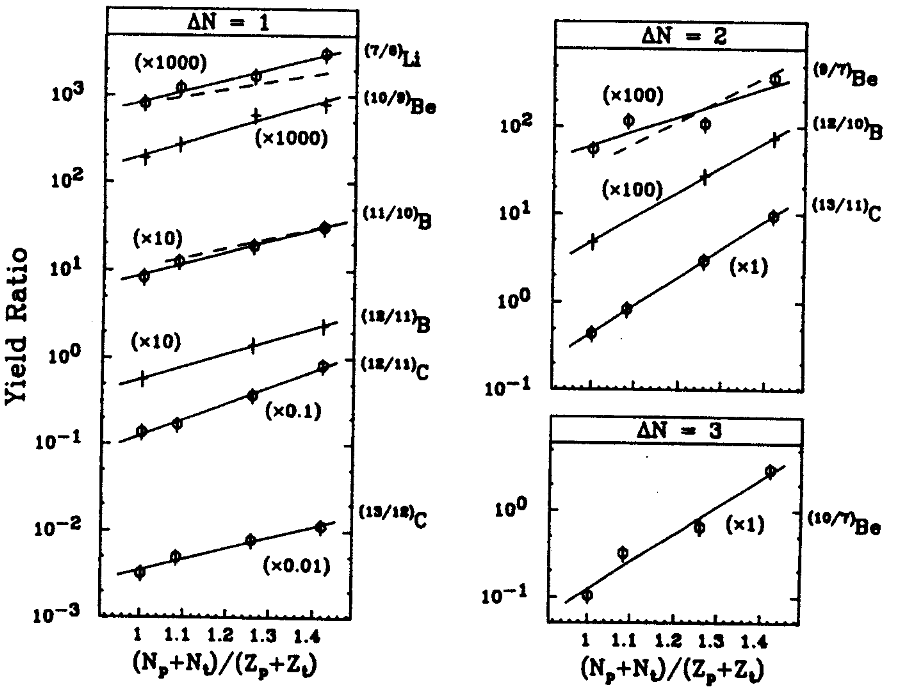

Fig. 1. Isotope yield ratios vs. neutron-to-proton ratio of the combined system, projectile (p)-plus-target (t). The points are the data, the solid straight lines are fits to them, and the dashed straight lines are fits to the data of Ref. 1. ΔN, the difference in the number of neutrons in the two isotopes of a ratio, is one for the six ratios at the left, two for the three ratios at the upper right, and three for the one ratio at the lower right. For clarity, the data and fits have been multiplied by various factors before plotting; the factors are given in parentheses.

figure has the $\Delta N=1$ cases, the upper right part the $\Delta N=2$ cases, and the lower right the one case for $\Delta N=3$. The solid lines, which are straight-line fits to the data, illustrate the exponential dependence of yield ratio on N/Z--the same type of dependence found by Wada et al.[1] Indeed, the slopes, and even the absolute values, of the lines fitting the data of Wada et al. are similar to ours. Their fits are represented by the three dashed lines in Fig. 1. (The dashed line in the upper right part of the figure, copied from Ref. 1, is for the collection of isotopes ^{11}Be rather than for the single isotope ^{9}Be.) The increasing steepness of the lines with increasing ΔN is in overall, but not in quantitative, agreement with Eq. 1.

It is clear that Eq. 1 fits our data about as well as they fitted the somewhat more limited data set of Wada et al. Perhaps this is surprising since the latter experiment was done at 84 MeV/nucleon and ours at only 35 MeV/nucleon. If the higher energy data are to be understood in terms of a statistical multifragmentation model, is the model also valid at 35 MeV/nucleon?

We would like to thank H.W. Barz and H. Schulz for helpful discussions.

a. Eötvös Lorand University, Budapest
b. Central Research Laboratory for Physics, Budapest

References

1. R. Wada, K.D. Hildenbrand, U. Lynen, W.F.J. Müller, H.J. Rabe, H. Sann, H. Stelzer, W. Trautmann, R. Trockel, N. Brummund, R. Glasow, K.H. Kampert, R. Santo, E. Eckert, J. Pochodzalla, I. Bock and D. Pelte, Phys. Rev. Lett. 58, 1829 (1987).
2. H.W. Barz, H. Schulz, J.P. Bondorf, J. Lopez and K. Sneppen, Phys. Lett. B 211, 10 (1988).
3. A. Kiss, F. Deak, Z. Seres, G. Caskey, A. Galonsky, B. Remington and L. Heilbronn, Nucl. Phys. A499, 131 (1989).
4. F. Deak, A. Kiss, Z. Seres, A. Galonsky, L. Heilbronn and H.R. Schelin, Phys. Rev. C 42, 1029 (1990).

NEUTRON INCLUSIVE MEASUREMENTS OF ^{36}Ar + Ag REACTIONS AT 35 MeV/NUCLEON

D. Sackett, A. Galonsky, C.K. Gelbke, H. Hama, L. Heilbronn D. Krofcheck, W. Lynch, H.R.Schelin, M.B. Tsang, X. Yang, F. Deák,[a] A. Horvath,[a] A. Kiss,[a] Z. Seres,[b] J. Kasagi,[c] T. Murakami.[d]

Using a 35 MeV per nucleon ^{36}Ar^{11+} beam provided by the K500 Cyclotron at Michigan State University, we have measured inclusive neutron spectra from the reaction Ag(^{36}Ar,n) at angles of 15°, 30°, 45°, 60°, 120°and 160°. The detectors and the measurement technique are described in detail in ref. 1. Figure 1 shows the double differential neutron cross section data. It is the behavior of the energy spectra that justifies a moving source analysis. At 45° and 60° the spectra appear to be superpositions of two distinct components which vary exponentially with energy. In terms of a nuclear temperature, the low energy neutron data possess a steeper slope, therefore indicating a cooler source. The higher energy neutrons stem from a hotter source, because the slope of the data is much flatter. The spectra at 120° and 160° decrease exponentially with increasing energy. Because the data at 120° and 160° have such similiar magnitudes, it can be inferred that the cooler source is moving slowly enough to provide nearly isotropic

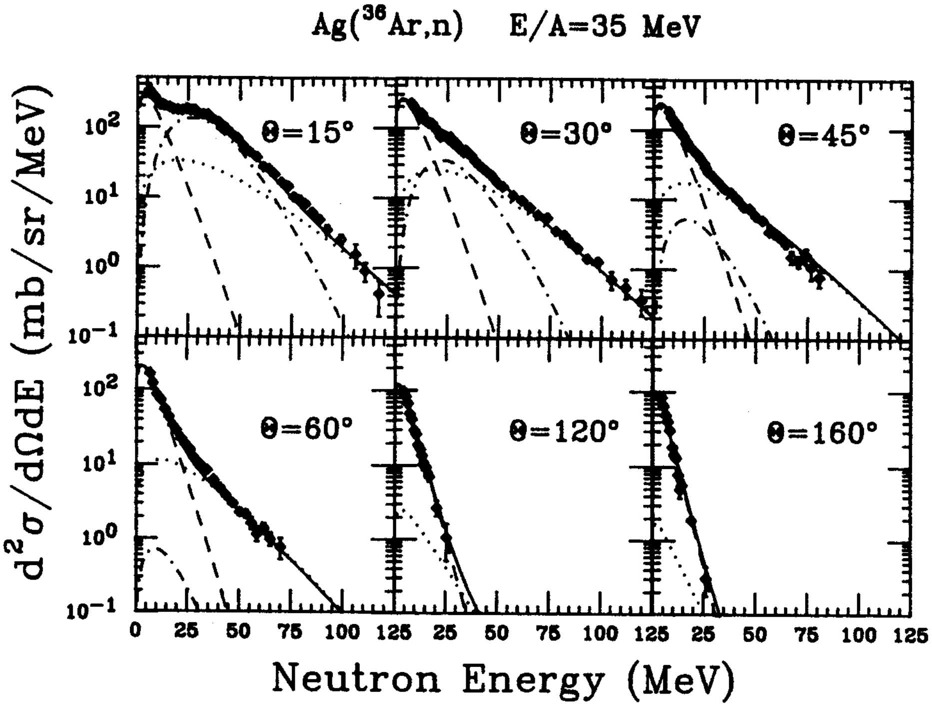

Figure 1: The neutron energy spectra at six angles. The solid lines are the fits using three thermal sources. The dot-dashed line is the contribution from the projectile-like source, the dotted line from the intermediate rapidity source, and the dashed line from the target-like source.

emission. The enhancement in the 15° spectrum arises from rapidly moving sources created by peripheral collisions, so their contribution appears only at forward angles.

To proceed with the fitting, it is assumed that the sources are Maxwellian in nature and emit neutrons isotropically in their own rest frames. Assuming volume emission, the neutron distribution in a source rest frame is:

$$\frac{d^2\sigma_n}{dE'd\Omega'} = \frac{N\sqrt{E'/\pi}}{2\pi T^{3/2}} \exp\left[\frac{-E'}{T}\right]$$

Here E' is the neutron energy in the source rest frame, Ω' is the solid angle in the source rest frame, T is the temperature in MeV and N is the neutron production cross section in barns. E' is related to the lab neutron energy E by:

$$E' = E + \epsilon - 2\sqrt{\epsilon E}\cos\theta$$

where ϵ is the kinetic energy per nucleon of the source and θ is the laboratory scattering angle. Summing over three sources, the parameterization in the laboratory frame of reference takes the form:

$$\frac{d^2\sigma_n}{dEd\Omega} = \sum_{i=1}^{3} \frac{N_i\sqrt{E/\pi}}{2\pi T_i^{3/2}} \exp\left[-\left[\frac{E - 2\sqrt{\epsilon_i E}\cos\theta + \epsilon_i}{T_i}\right]\right]$$

The nine fit parameters are N, T and ϵ for each source. The fitting was performed using a χ^2 minimization procedure. The χ^2 per degree of freedom was 3.71. Uncertainties correspond to the change in a parameter that increases χ^2 by 1, with all other parameters fixed at their optimum values.[2]

Table 1 summarizes the best fit values of the parameters, and Figure 1 displays the data and the overall fit. The values of the fit parameters confirm the characterisitics attributed to each source. Thus, the moving source analysis, while providing a good fit to the data, also contains a reasonable description of the reaction dynamics. For example, there is a slowly-moving, target-like source (TLS) that de-excites via neutron and charged-particle evaporation, and a hotter ($T \approx 11$ MeV) intermediate rapidity source (IRS) moving with $V \approx V_{beam}/2$ that de-excites in a similar manner. Finally, there is a projectile-like source (PLS) moving with a speed close to the beam velocity. Because the PLS originates from peripheral collisions, it must be noted that the assumption of thermal equilibrium, although convenient, is an oversimplification.[3] This source is included in the parameterization because it provides a useful fit to the spectra at the most forward angles.

The remaining parameter, the neutron cross section N_i, is related to the multiplicity of the ith

source as $M_i = N_i/\sigma_{tot}$. The total reaction cross section is calculated from:

$$\sigma_{tot} = \pi[r_0(36^{1/3} + 108^{1/3})]^2 = 3.40\,\text{b. with } r_0 = 1.29\,\text{fm.}^1$$

A 10% error is assumed in σ_{tot}.[1] The calculated neutron multiplicities are also shown in Table 1. The multiplicities are also meaningful in terms of the moving source analysis. The low-energy part of the spectrum is well described by a purely exponential function of energy, and is attributed to a target-like remnant that de-excites via neutron and charged-particle evaporation. Coincidence measurements of neutrons and intermediate mass fragments ($3 \leq Z \leq 5$)[4] or neutrons and fission fragments[5] for systems with similar targets and beam energies find TLS multiplicites between 5 and 7, in agreement with our result of 5.6. The intermediate-rapidity source models the early stage of the reaction, where nucleon-nucleon collisions largely determine the spectrum. For beam energies around 30-35 MeV/nucleon, neutron multiplicities ranging from one to three have been found[4, 5] , in agreement with our value of 1.1.

The most direct comparison can be made with the data of Schelin *et al.*[3] They have measured inclusive neutron spectra for ^{14}N on Ag at 35 MeV per nucleon. Table 1 compares their moving source parameters (in parenthesis) with ours. The final column in Table 1 represents the kinetic energy of the neutrons from the ith source, evaluated in the center of mass system. This kinetic energy is calculated from:

$$E'_{n_i} = \int_0^\infty \frac{dN_i(E')}{dE'} E' dE'$$

$\frac{dN_i}{dE'}$, the number of neutrons/MeV from the ith source, is:

$$\frac{dN_i}{dE'} = \frac{1}{\sigma_{tot}} \left(\frac{d\sigma_n}{dE'}\right)_i$$

where σ_{tot} is the total reaction cross section defined previously. Explicitly, the integral appears as:

$$E'_{n_i} = \frac{2N_i}{\sqrt{\pi}\sigma_{tot}T_i^{3/2}} \int_0^\infty E'^{3/2} e^{-E'/T_i} dE' = \frac{3}{2} M_i T_i$$

For the target-like source, the multiplicities and temperatures are approximately the same for both systems. Since the temperature of the source is directly related to it's excitation energy, this is a surprising result when the available energy in the center of mass reference frame (E'_{cm}) is considered. For the nitrogen projectile, E'_{cm} is 434 MeV, and for the argon beam E'_{cm} is 945 MeV, an increase by a factor of

Table 1

Source	T (MeV)	ϵ (MeV/nucleon)	N (barns)	Multiplicity	E'_n (MeV)
TLS	4.2 ± 0.3 (4.0 ± 0.2)	0.56 ± 0.13 (0.45 ± 0.02)	19.1 ± 1.7 (12.2 ± 1.1)	5.6 ± 0.7 (4.5 ±0.6)	35 ± 7 (27 ± 6)
IRS	11.4 ± 1.3 (11.1 ± 0.6)	11.77 ± 2.0 (12.8 ±0.5)	3.9 ± 0.5 (2.32 ± 0.2)	1.1 ± 0.2 (0.86 ± 0.11)	20 ± 6 (14 ± 3)
PLS	3.6 ± 0.4 (2.2 ± 0.3)	24.6 ± 1.8 (30.1 ± 3.6)	3.2 ± 0.4 (0.71 ± 0.06)	0.9 ± 0.1 (0.26 ± 0.04)	5 ± 1 (1 ±0.3)
Totals				7.6 ± 0.7 (5.6 ± 0.7)	60 ± 9 (42 ± 7)

Table 1: Temperatures, source velocities, source strengths and multiplicities for a three-source fit to the neutron spectra for the reaction ^{36}Ar(Ag,n). The results of Schelin *et al.* (ref. 1) are in parentheses. The final column is the total kinetic energy of the neutrons from the i^{th} source.

2.2. It would seem that a large increase in excitation energy would create a more highly excited TLS, thus causing signifcant changes in the temperature and multiplicity parameters. The data imply that this is not happening. The source multiplicities and temperatures (and therefore excitation energies) are essentially the same for each projectile. Also, the total kinetic energy of the emitted neutrons (final column of Table 1) only changes from 27 MeV (nitrogen beam) to 35 MeV for the argon beam, an increase of about 30%. One possible explanation is that, for either projectile, the TLS evaporates it's lightly bound neutrons, but as it becomes more neutron deficient, separation energies increase such as to suppress further emission. Another factor is that with a larger projectile (argon) the geometric probability of incomplete fusion versus complete fusion is greater. By incomplete fusion, we mean any collision where a significant projectile-like spectator is formed. Of course, at higher excitation energies, new fragmentation decay channels may become available such that neutron evaporation is de-emphasized. In fact, fragment multiplicities (M_{frag}) for both projectiles on a silver target have recently been measured.[7] For the nitrogen projectile, M_{frag}=0.06 while for the argon beam, M_{frag}=0.33, an increase by a factor of 5.5.

The IRS describes the contribution to the neutron spectra from the early part of the interaction between projectile and target, where individual nucleon-nucleon collisions are important. In this regime, the velocity of the projectile nucleons is a major factor in determining the resulting neutron kinetic energy spectra. For the experiments with argon and nitrogen projectiles, the nucleon velocities are identical, so similar kinetic energy spectra are expected. Because the source temperature reflects the resulting kinetic energy spectra, the temperatures should therefore be similar. From Table 1, this is certainly the case. For argon and nitrogen projectiles the IRS temperatures are 11.4 and 11.1 MeV, respectively. Because the argon projectile is more massive and therefore contributes more kinetic energy to the target, the energy will be dissipated over a larger region of the target. Thus the source size is expected to increase, but not the temperature.

Again referring to Table 1, we find that there is only a small increase in the IRS multiplicity (from 0.86 to 1.1) for the Ag(^{36}Ar,n) reaction, compared to the Ag(^{14}N,n) reaction. This is a surprising result, considering that IRS neutron spectra are largely determined by nucleon-nucleon collisions, and that there are $\sim$ 2.6 times as many nucleons in the argon projectile. Possibly the same effects that suppress the TLS multiplicity exist here also. Refering to the data of Hama *et al.*[3] , the fragment multiplicities for the nitrogen and argon beams are 0.08 and 0.38 respectively, an increase by about a factor of 5.

Since the main difference between the Ar+Ag and N+Ag systems is the size of the projectile, it should not be surprising that the fit parameters for the PLS are affected the most. The multiplicity for the argon projectile is $\sim$ 3 times greater, which should be expected since there are $\sim$ 2.6 times as many neutrons in the argon projectile. Also, the temperature and the total neutron kinetic energy (E_n') are higher, whereas the source velocity is a bit lower. This implies a greater exchange of energy and momentum between target and projectile for grazing collisions.

We have measured the inclusive neutron spectra for the reaction Ag(^{36}Ar,n) at 35 MeV/nucleon. The energy spectrum at several angles can be fitted with three moving sources, and the resulting fit parameters are physically reasonable. Comparing our temperatures, multiplicites and total neutron kinetic energies to values found in previous lower- energy work, we find that a large increase in available excitation energy does not manifest itself in more-highly-excited sources and higher neutron multiplicities. One possible explanation is that there may be alternative modes of de-excitation at higher energies. Further studies measuring both inclusive and exclusive neutron spectra over ranges of bombarding energies, with the same target and projectile, would provide the systematics to study this interesting effect.

a. Eötvö Lorand University, Budapest

b. Central Research Laboratory for Physics, Budapest

c. Tokyo Institute of Technology

d. Kyoto University

References

1. H.R. Schelin *et al.*, Phys. Rev. C39 (1989), p 1827.
2. P.R. Bevington, Program in CURFIT in *Data Reduction and Error Analysis for the Physical Sciences* (McGraw-Hill, New York, 1969), p 237.
3. A. Kiss *et al.*, Phys. Lett. B184 (1987), p 149.
4. C. Bloch *et al.*, Phys. Rev. C37 (1988), p 2469.
5. J. Galin, Proceedings of the Third International Conference on Nucleus-Nucleus Collisions, Saint-Malo, France, 1988.
6. D. Hilscher *et al.*, Phys. Rev. C36 (1987), p 208.
7. H. Hama *et al.*, private communication.

TESTS OF THE THERMAL NATURE OF INTERMEDIATE-MASS FRAGMENT PRODUCTION USING NEUTRON UNBOUND STATE POPULATIONS

L. Heilbronn, F. Deak[a], A. Galonsky, C. K. Gelbke, J. Kasagi[b], A. Kiss[a], W. G. Lynch, T. Murakami[c], B. A. Remington[d], D. Sackett, H. Schelin[e], Z. Seres[f], and M. B. Tsang

An important property of intermediate-energy (E/A ≈ 20-200 MeV) heavy-ion reactions is the production of intermediate-mass fragments (for this report, $3 \leq Z \leq 7$, $6 \leq A \leq 14$, referred to as IMFs). An analysis of IMF singles spectra from this energy range suggests that two types of reaction mechanisms are responsible for their production; a quasielastic (QE) mechanism and a deep-inelastic (DI) mechanism.[1] Perhaps the most significant difference between QE and DI IMF spectra is that QE spectra seem to be produced from a non-statistical mechanism, whereas DI IMFs appear to be produced from a source in thermal equilibrium. In general, QE spectra are described by various nucleon exchange models,[1,2] whereas DI spectra are parameterized using a moving-source model which assumes that light particles and fragments are emitted from a hot, moving source that is in thermal equilibrium, and that the kinetic energy distribution of the emitted particles and fragments is governed by a Maxwell velocity distribution. For the system studied in this report (^{14}N + Ag, E/A = 35 MeV), IMFs come from a source with a velocity roughly one-third of the beam velocity and with a source temperature of about 13 MeV.[3,4]

In order to explore further the thermal nature of DI IMF production, a large number of both particle-bound excited states and particle-unbound states in IMFs have been detected in several intermediate-energy systems (see Ref. 5 and references therein). The measured populations of these states can be used to calculate temperatures from a Boltzmann population distribution, where the population ratio of two states of the same nucleus is related to the Boltzmann temperature (T) in the following way:

$$R = \frac{2J_1+1}{2J_2+1} \exp(-\Delta E/T). \qquad (1)$$

R is the ratio of the population of state 1 to the population of state 2, J_1 and J_2 are the state spins, and ΔE is the difference in level energy between state 1 and state 2. If it is assumed that excited, DI IMFs come from a thermal source, then the population ratio gives the temperature of that source, just as IMF kinetic energy spectra also give that temperature. After correcting for sequential feeding[6] the temperatures deduced from population ratios range between 3 and 5 MeV, independent of the system used. Note that the temperatures deduced from population ratios are much lower than the temperatures extracted from IMF spectra.

The fact that population temperatures do not change as the system changes, and the fact that there is a large discrepancy between spectral temperatures and population temperatures may lead one to question the assumption of a thermal production of IMFs. Perhaps the strongest evidence against a thermal production of excited IMFs comes from a group that has measured the populations of seven states in the same isotope.[7] They report that it is not possible to fit a single temperature to all seven populations, even after taking sequential feeding into account. Given these facts, it appears that the validity of assuming a thermal production is open to debate, and that more data will be needed to resolve this issue.

We have measured a total of 14 neutron-unbound state populations from the reaction ^{14}N + Ag at E/A = 35 MeV. This data complements a set of data of other excited-state populations measured for this system.[8-10] In this report we test the assumption of a thermal production of DI IMFs in two ways, using the measured neutron-unbound state populations. In one test we attempt a global fit to a large number of unbound/bound-state population ratios (referred to as "two-level ratios") using a single source temperature. In the other test we attempt to fit a single temperature to all of the populations of isotopes that had three or more measured populations (referred to as "multilevel populations").

For both of the tests, the populations are compared with the results from a sequential decay code calculation. The model calculation creates a primary, or "initial", population of IMFs in bound and unbound states, with all of the populations characterized by a single temperature. The decay of these fragments is then followed until a ground-state fragment is reached. The decay of a fragment from the initial distribution may follow several steps before finally decaying to a ground-state fragment. The populations of the "final step" states, i.e., the populations of the levels that decay directly to a bound state of a fragment, are also calculated in the model. Population ratios, such as the ones measured in the laboratory, are then calculated using the final step unbound-state populations and the final ground-state populations predicted by the model. More details of the model may be found in Ref. 9.

Two-Level Population Ratios

In total, eleven unbound-state populations were determined from seven isotopes whose bound-state populations were also determined. The ratios of an unbound-state population to its corresponding bound-state population are shown in Fig. 1. The data are labeled with the appropriate unbound-state energy. The error bars include experimental and systematic errors. The lefthand plot in Fig. 1 is for IMFs at 15°. The open symbols are for QE ratios, and the solid symbols are for the DI ratios. The middle plot of Fig. 1 shows the data for DI IMFs at 31° and the righthand plot shows the data at 64°.

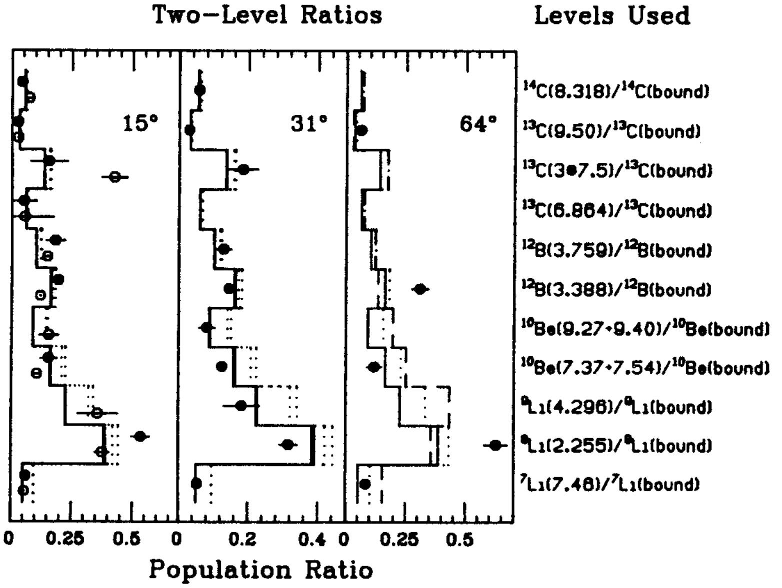

Fig. 1 - The lefthand plot contains the population ratios at 15° with the solid symbols representing the DI data and the open symbols representing the QE data. The middle plot is for DI IMFs at 31°, and the righthand plot is for DI IMFs at 64°. The solid histograms in every plot indicate the ratios calculated from a sequential feeding model for $T_{source} = 2.5$ MeV, and the dotted histograms indicate the calculated ratios for $T_{source} = 3.5$ MeV. The dashed line in the righthand plot indicates the ratios predicted by the sequential feeding model for $T_{source} = 6.0$ MeV. The bound states and unbound states used to calculate the ratios are shown on the righthand side of the figure.

Populations are identified as DI or QE by the IMF's kinetic energy.[9] At 15°, the region of kinetic energy taken to be DI is 6-15 MeV/nucleon or, when possible, 6-10 MeV/nucleon. All of the data above 15 MeV/nucleon at 15° is identified as QE. The DI region at 31° was taken to be all energies above 6 MeV/nucleon, except for the 3.388-MeV and 3.756-MeV states in ^{12}B and the 7.37-MeV + 7.54-MeV group of states in ^{10}Be, where the DI region was taken to be 6-15 MeV/nucleon. All of the data at 64° is DI.

The histograms in Fig. 1 represent the population ratios calculated with the final bound-state and unbound-state populations predicted by the sequential decay model. The dotted histograms show the predictions of the population ratios for an initial source temperature of 3.5 MeV, and the solid histograms show the predictions for a temperature of 2.5 MeV. Note that for each initial source temperature there is a pair of histograms showing the prediction of the measured population ratio. The pair of histograms represents the uncertainty in the calculation due to unknown values of level spin, parity, and isospin. The dashed line in the righthand plot is for a source temperature of 6.0 MeV.

Looking at the DI population ratios at 15° (solid symbols), it is seen that seven of the nine ratios are fitted by the model predictions for initial temperatures between 2.5 and 3.5 MeV. At 31°, eight of the ten DI population ratios are fitted by the model calculations for source temperatures between 2.5 and 3.5 MeV. Based on the results for DI ratios at 15° and 31°, it appears that the data is consistent with production from a thermal source whose temperature is between 2.5 and 3.5 MeV. However, the data at 64° cannot be fitted by the model predictions, even for a range of 2.5 to 6 MeV. Only one point, the point for the 9.5-MeV state in ^{13}C, agrees with the model predictions with source temperatures between 2.5 and 3.5 MeV.

It is interesting to note that, for the most part, the measured DI and QE population ratios at 15° are similar. The noteable exceptions are the group of states near 7.5 MeV in ^{13}C, the 3.388-MeV state in ^{12}B, and the 7.37-MeV + 7.54-MeV pair of states in ^{10}Be. Otherwise, it appears that the population ratios for QE IMFs are similar to those for DI IMFs.

Multilevel Populations

Another test which can be applied to the DI population data to see if they are consistent with emission from a thermal source is to check whether three or more populations from the same nucleus can be fitted with a single temperature. Figure 2 shows a plot of the natural logarithm of the population (divided by the appropriate spin factor) of each of the three unbound states and of the bound states

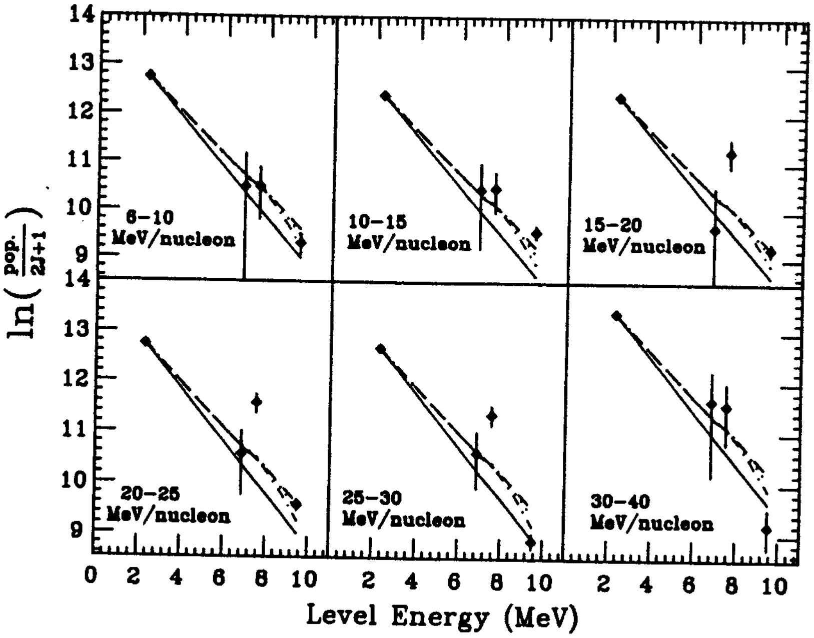

Fig. 2 - Plots of the natural logarithm of the populations of the detected levels in ^{13}C versus the level energy for various cuts on fragment kinetic energy. The solid, dashed, dotted, and dot-dashed lines in each plot show the predictions from the sequential feeding model for initial source temperatures of 2, 3, 4, and 5 MeV, respectively.

detected for ^{13}C at 15° for the indicated cuts on fragment energy. Each point is plotted at its appropriate level energy. All of the bound states were treated as a single state whose level energy is 2.3 MeV, and whose effective spin factor (2J+1) is 12.22.[5] The solid, dashed, dotted and dot-dashed lines in each plot indicate the predicted populations from the sequential feeding model for initial temperatures of 2, 3, 4 and 5 MeV, respectively. The data for 6-10 MeV/nucleon is fitted with the model calculations using initial temperatures of 3, 4, and 5 MeV. The data for 10-15 MeV/nucleon is nearly fitted with the model calculation. For ^{13}C the data below 15 MeV/nucleon is dominated by DI processes, and it appears that for the data in this region the measured populations are indicative of a thermal reaction mechanism. Above 15 MeV/nucleon none of the data is fitted with the model calculation, although the data from 30-40 MeV/nucleon is nearly fitted. This is consistent with the assumption of a nonthermal reaction mechanism for the production of QE IMFs.

Figure 3 shows the plot of the logarithm of three populations in ^{12}B, the 3.76-MeV state, the 3.388-MeV state, and the bound states. The bound states were treated as the a single state with a level-energy of 1.13 MeV and an effective spin factor of 16.35. The left plot in Fig. 3 is for 15° and 6-15 MeV/nucleon (DI), the middle plot is for 15° and 15-40 MeV/nucleon (QE), and the right plot is for 31° and 6-15 MeV/nucleon (DI). The lines represent the same temperatures as in Fig. 2. As in Fig. 2, the QE data (middle plot) is not fitted by any of the model predictions. However, none of the DI data is fitted, either, which is in contrast to the results presented in Fig. 2, where the DI data is fitted and the QE data is not.

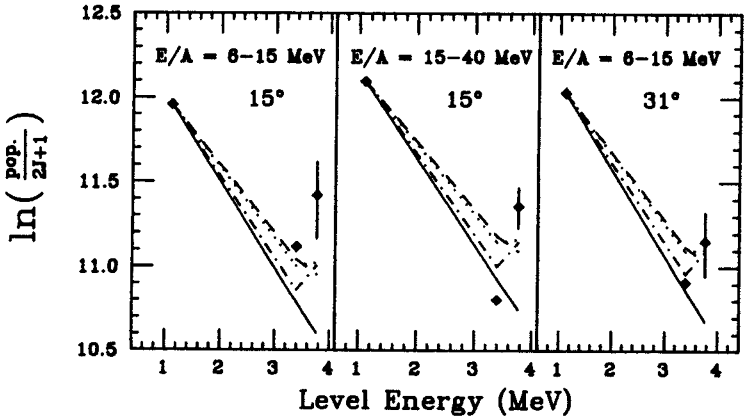

Fig. 3 - Plots of the natural logarithm of the populations of the detected levels in ^{12}B versus the level energy for various cuts on IMF energy at 15° and 31°. The lines have the same meaning as in Fig. 2.

Figure 4 shows plots of the logarithm of three populations in ^{10}Be, the 7.37-MeV + 7.54-MeV group of states, the 9.27-MeV + 9.4-MeV group of states, and the bound states. The bound states were plotted as a single state with an energy of 3.7 MeV and an effective spin factor of 15.95. The left plot is for 15° and kinetic energies above 15 MeV/nucleon (QE), the middle plot is for 31° and energies below 15 MeV/nucleon (DI), and the right plot is for 31° and energies above 15 MeV/nucleon (QE). The

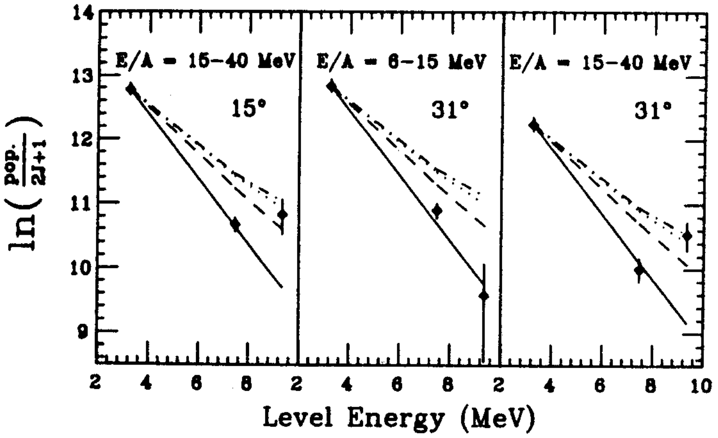

Fig. 4 - Plots of the natural logarithm of the populations of the detected levels in ^{10}Be versus the level energy for various cuts on IMF energy at 15° and 31°. The lines have the same meaning as in Fig. 3

lines represent the same temperatures as in Figs. 2 and 3. As in Figs. 2 and 3 the QE data cannot be fitted with a single temperature. It appears that the DI data can be fitted with a temperature between 2 and 3 MeV.

In regards to the nature of the DI reaction mechanism, the results from the two-level and multilevel data are not clear. Some of the DI data can be fitted with a thermal model, but there are some exceptions which are not fitted. What this set of data may indicate is that the DI reaction mechanism may indeed be thermal in nature, but that there are other effects present during the reaction which are not accounted for in the model which can alter some of the measured populations such that they appear to be nonthermal. The data may also indicate that while feeding calculations like the one used here may be generally correct, it may not be correct for every final state.

a. Department of Atomic Physics, Eötvös University, Budapest 114, Hungary H-1088
b. Department of Physics, Tokyo Institute of Technology, O-Okayama, Meguro-Ku, Tokyo, Japan
c. Department of Physics, Kyoto University, Kitasherakawa, Kyoto 606, Japan
d. Lawrence Livermore National Laboratory, Livermore, California 94450
e. Centro Tecnico Aeroespacial and FAPESP, Brazil
f. Hungarian Academy of Sciences, KFKI, Budapest 114, Hungary H-1525

References

1. A. Kiss, F. Deak, Z. Seres, G. Caskey, A. Galonsky, B. Remington and L. Heilbronn, Nucl. Phys. **A499**, 131 (1989).
2. J. Wilczynski and K. Siwek-Wilczynska, Phys. Rev. C 41, R1917 (1990).
3. C. Bloch, W. Benenson, A.I. Galonsky, E. Kashy, J. Heltsley, L. Heilbronn, M. Lowe, R.J. Radtke, B. Remington, J. Kasagi, and D.J. Morrissey, Phys. Rev. C **37**, 2469 (1988).
4. F. Deak, A. Kiss, Z. Seres, A. Galonsky, L. Heilbronn, and H. R. Schelin, Phys. Rev. C **42**, 1029 (1990).
5. L. Heilbronn, Ph.D. thesis, Michigan State University, 1991.

6. D. Hahn and H. Støcker, Phys. Rev. C **35**, 1311 (1987).
7. T.K. Nayak, T. Murakami, W.G. Lynch, K. Swartz, D.J. Fields, C.K. Gelbke, Y.D. Kim, J. Pochodzalla, M.B. Tsang, H.M. Xu, F. Zhu and K. Kwiatkowski, Phys. Rev. Lett. **62**, 1021 (1989).
8. D. Fox, D.A. Cebra, J. Karn, C. Parks, A. Pradhan, A. Vander Molen, J. van der Plicht, G.D. Westfall, W.K. Wilson and R.S. Tickle, Phys. Rev. C **38**, 146 (1988).
9. H.M. Xu, W.G. Lynch, C.K. Gelbke, M.B. Tsang, D.J. Fields, M.R. Maier, D.J. Morrissey, T.K. Nayak, J. Pochodzalla, D.G. Sarantites, L.G. Sobotka, M.L. Halbert and D.C. Hensley, Phys. Rev. C **40**, 186 (1989).
10. C. Bloch, W. Benenson, A.I. Galonsky, E. Kashy, J. Heltsley, L. Heilbronn, M. Lowe, B. Remington, D.J. Morrissey and J. Kasagi, Phys. Rev. C **36**, 203 (1987).

DEPENDENCE OF POPULATION RATIOS ON FRAGMENT KINETIC ENERGY FOR ^{14}N + Ag, E/A = 35 MeV REACTIONS

L. Heilbronn, F. Deak[1], A. Galonsky, C. K. Gelbke, J. Kasagi[2], A. Kiss[1], W. G. Lynch, T. Murakami[3], B. A. Remington[4], D. Sackett, H. Schelin[5], Z. Seres[6], and M. B. Tsang

The populations of excited states of quasielastically produced intermediate-mass fragments (referred to as QE IMFs), especially the populations of excited-state IMFs with large kinetic energies, should bear information on the partition of excitation energy between reaction partners.[1] The dependence of IMF excited-state populations on IMF kinetic energy is seen as an important test of nucleon-exchange models[1-3] used to describe QE IMF production. One group has reported on the dependence of the ratio of specific gamma-emitting states' populations to their corresponding fragment singles populations on kinetic energy.[1] They show that for QE IMFs with a mass lower than the mass of the beam (stripping reactions) the ratio is essentially constant, whereas for QE IMFs with a mass higher than the mass of the beam (pickup reactions), the ratio increases as the kinetic energy increases. Another group[4] has reported on the dependence of the ratio of the population of the 3.388-MeV state in ^{12}B to its corresponding bound states population on kinetic energy, and they report that the ratio decreases as the kinetic energy increases, even though in this case the detected fragment had a smaller mass than the mass of the beam. Note that these two reports on the dependence of IMF excitation as a function of kinetic energy for QE IMFs with a mass below the mass of the beam are different from each other. It is not known if this difference is due to the fact that the two reports came from different reaction systems (^{14}N + ^{164}Dy at E/A = 20 MeV for Ref. 1 and ^{14}N + Ag at E/A = 35 MeV for Ref. 4) or is due to the fact that bound-state populations were measured in one experiment[1] and unbound-state populations were measured in the other.[4] In any case, there is a need for more of this type of data on QE IMFs.

Just as the dependence of population ratios on IMF kinetic energy can give detailed information on the production of QE IMFs, this dependence can also yield important information on the nature of the thermal source producing deep-inelastic intermediate-mass fragments (referred to as DI IMFs), assuming they are produced by such a source. For example, if one assumes that this thermal source behaves like a source of infinite extent, one would expect the value of the population ratio to be constant as a function of kinetic energy. On the other hand, if the source is small enough, the effects of cooling from particle emission may give an altogether different dependence of the population ratio on kinetic energy. One can imagine that as a finite-size source emits particles and fragments, it will cool and subsequently emit fragments whose kinetic energy distributions and state populations will be characteristic of the lower temperature. Because of this, IMFs with low values of kinetic energy would, on the average, come from the later, cooler stages of the reaction than IMFs with higher values of kinetic energy. Thus, the value of the population ratio would increase as IMF kinetic energy increased. An argument can be made that a finite-sized source which is vulnerable to the effects of evaporative cooling is <u>not</u> a source in thermal equilibrium, but in any case the dependence of population ratios on IMF kinetic energy will add more information on the nature of the reaction mechanism producing DI IMFs.

The dependence of the ratio of an unbound-state population to the bound-state population on IMF kinetic energy is reported here for the 7.456-MeV state in ^{7}Li, the 2.255-MeV state in ^{8}Li, the 3.388-MeV state in ^{12}B, and the 9.5-MeV state and 7.5-MeV group of states in ^{13}C in Figs. 1-4, respectively. The upper plots show the population ratios versus kinetic energy, while the lower plots show the corresponding singles spectra. In Fig. 1, the filled points show the data after correcting the inclusive spectra for ^{8}Be contamination, and the open symbols show the data before the correction. The top plot in Fig. 4 is for the group of three states near 7.5-MeV in ^{13}C, and the middle plot is for the 9.5-MeV state. For reference, a temperature scale computed using the Boltzmann population distribution relation is included in the upper plots of Figs. 1-3. The numbers above and below the

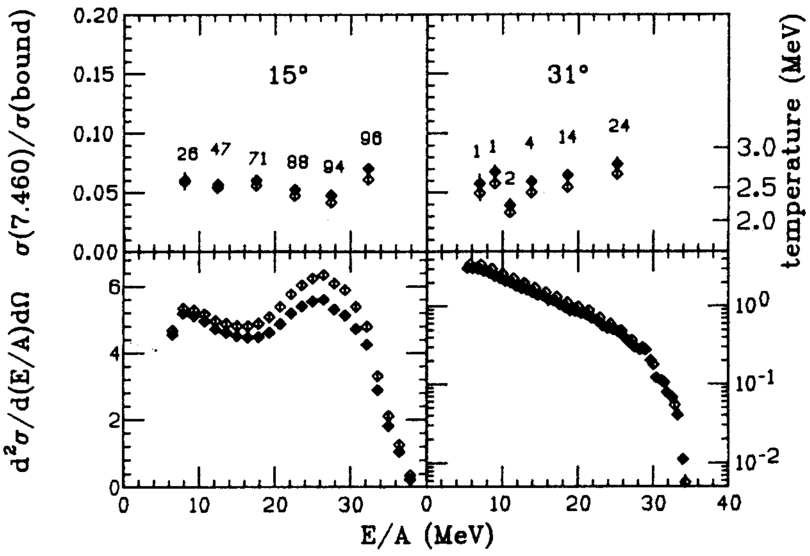

Fig. 1 - The upper plots show the ratio of the population of the neutron-unbound 7.46-MeV state in ^{7}Li to the ^{7}Li bound-state population as a function of fragment kinetic energy at 15° and 31°. Open symbols represent the data before correcting for ^{8}Be contamination, and filled symbols represent the data after the correction. The lower plots show the ^{7}Li singles spectra at 15° and 31°. The open and filled symbols have the same meanings as for the upper plots. The numbers in the upper two plots indicate the percentage of QE ^{7}Li in the bound-state yield for the corresponding energy bin.

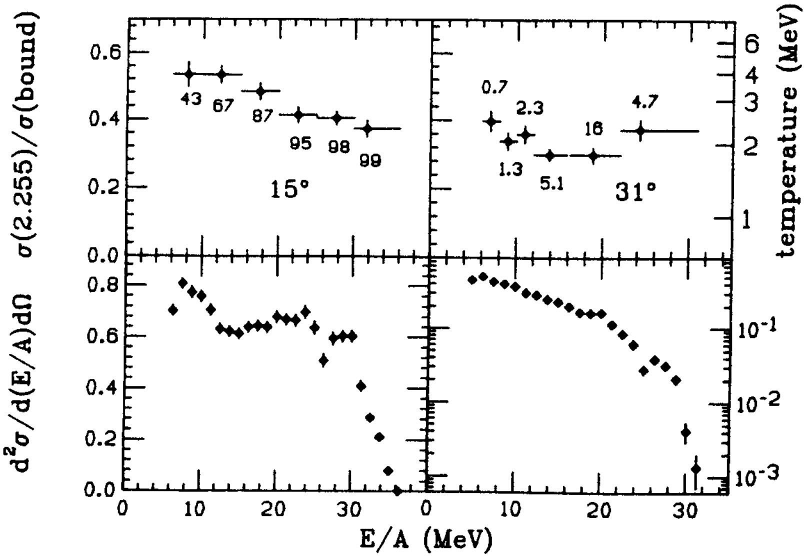

Fig. 2 - The upper plots show the ratio of the population of the neutron-unbound 2.255-MeV state in ^{8}Li to the ^{8}Li bound-state population as a function of fragment kinetic energy at 15° and 31°. The lower plots show ^{8}Li singles spectra at 15° and 31°. The numbers in the upper two plots indicate the percentage of QE ^{8}Li in the bound-state yield for the corresponding energy bin.

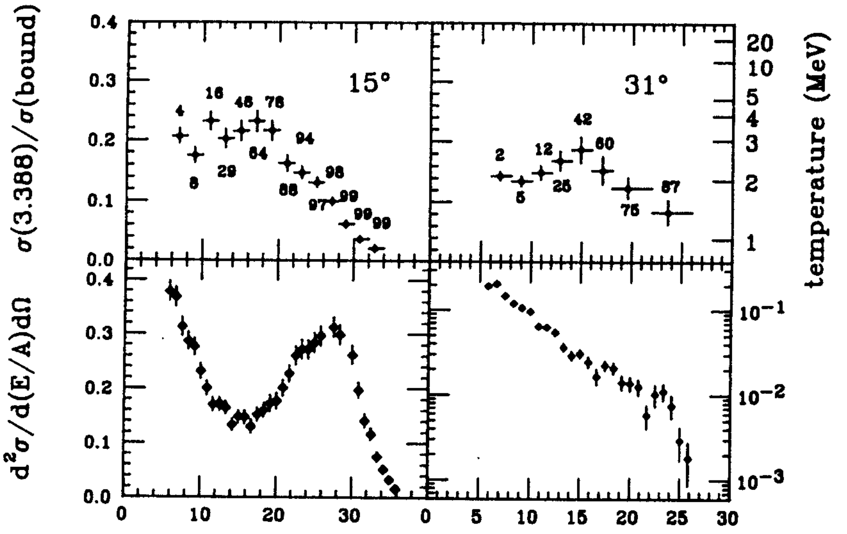

Fig. 3 - The upper plots show the ratio of the population of the neutron-unbound 3.388-MeV state in ^{12}B to the ^{12}B bound-state population as a function of fragment kinetic energy at 15° and 31°. The lower plots show ^{12}B singles spectra at 15° and 31°. The numbers in the upper plots indicate the percentage of QE ^{12}B in the bound-state yield for the corresponding energy bin.

data points in the upper plots indicate the percentage of QE data in the bound-state yield at a particular energy gate, as determined from an analysis of IMF singles spectra.[5]

QE IMFs

The dependence of the population ratio on IMF kinetic energy for QE events may be seen in Figs. 1-4 for large kinetic energies. It is interesting to note that for the two isotopes with a mass close to the mass of the projectile, ^{12}B and ^{13}C (Figs. 3 and 4), the ratio decreases as the fragment kinetic energy increases, and it appears that the ratio goes to zero as the fragment velocity approaches the beam velocity. However, for the two isotopes with about half the mass of the projectile, ^{7}Li and ^{8}Li (Figs. 1 and 2), the ratio appears to be constant, or decreasing slightly, with the ratio still above zero for fragment velocities near the beam velocity. In terms of a nucleon-exchange model, the difference in the population ratio versus kinetic energy between IMFs

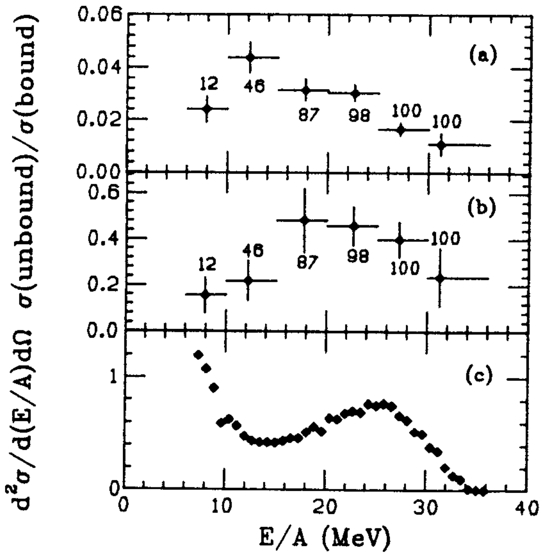

Fig. 4 - (a) and (b) show the population ratios of neutron-unbound states in ^{13}C to the ^{13}C bound states as a function of ^{12}C kinetic energy at 15°. In (a) the unbound state is at 9.50 MeV, and in (b) there are three unresolved unbound states at 7.49-MeV, 7.55-MeV, and 7.69-MeV. The numbers in (a) and (b) indicate the percentage of QE ^{13}C in the bound-state yield for the corresponding energy bin. (c) shows the ^{13}C singles spectrum at 15°.

with half-beam mass and near-beam mass is consistent with the picture of collisions with smaller impact parameter (hence more mixing between target and projectile nucleons) for the lower-mass IMFs. Even for IMF velocities near the velocity of the beam, one might expect that the lower-mass IMFs to be in a higher state of excitation than the higher-mass IMFs since a projectile which has lost half of its nucleons is much more deformed than a projectile that has lost only one or two nucleons.

The dependence of the population ratio versus kinetic energy was measured for the 6.8-MeV state in ^{11}B and the 4.4-MeV state in ^{12}C for projectilelike fragments created in the E/A = 20 MeV, ^{14}N + ^{164}Dy reaction, and it was found that the ratio was essentially constant with kinetic energy and above zero near the velocity of the beam.[1] These results are quite different from the results presented here for IMFs with similar mass, namely ^{12}B and ^{13}C. In fact, their results more closely resemble the results presented here for ^{7}Li and ^{8}Li. As stated earlier in this report, it is not known if the discrepancy between the results here and those of Ref. 1 is due to the different beam energy and target or due to the fact that one set of ratios is for unbound states, and the other is for bound states. Regardless, measurements such as these give an indication of the amount of excitation energy deposited in the QE fragment, and the dependence of the ratio on kinetic energy may bear important information on the details of models used to predict the production of QE IMFs, such as the nucleon-exchange model.[6]

DI IMFs

The kinetic energy dependence of the ratio of an unbound-state population to a bound-state population for DI IMFs may be seen in Figs. 1 and 4 at 31° and in Fig. 3 for low energies at 15° and

31°. The dependence of the ratio of the 2.255-MeV state population in ^{8}Li (Fig. 2) to the bound-state population on kinetic energy indicates a slightly decreasing or constant ratio with increasing kinetic energy. A constant ratio would be consistent with emission from a thermal source, assuming that effects due to evaporative cooling could be neglected. The data for the 7.46-MeV state in ^{7}Li (Fig. 1) and the 3.388-MeV state in ^{12}B (Fig. 3) are consistent with the dependence of the ratio on kinetic energy observed for the 2.255-MeV state in ^{8}Li, although there is clearly a need for data at lower fragment kinetic energies to firmly establish this dependence for DI IMFs.

1. Department of Atomic Physics, Eötvös University, Budapest 114, Hungary H-1088
2. Department of Physics, Tokyo Institute of Technology, O-Okayama, Meguro-Ku, Tokyo, Japan
3. Department of Physics, Kyoto University, Kitasherakawa, Kyoto 606, Japan
4. Lawrence Livermore National Laboratory, Livermore, California 94450
5. Centro Tecnico Aeroespacial and FAPESP, Brazil
6. Hungarian Academy of Sciences, KFKI, Budapest 114, Hungary H-1525

References

1. K. Siwek-Wilczynska, R. A. Blue, L. H. Harwood, R. M. Ronningen, H. Utsunomiya, J. Wilczynski, and D. J. Morrissey, Phys. Rev. C **32**, 1450 (1985).
2. P. J. Siemens, J. P. Bondorf, D. H. E. Gross, and F. Dickman, Phys. Lett. **36B**, 24 (1971).
3. J. Wilczynski and K. Siwek-Wilczynska, Phys. Rev. C **41**, R1917 (1990).
4. F. Deak, A. Kiss, Z. Seres, A. Galonsky, C. K. Gelbke, L. Heilbronn, W. Lynch, T. Murakami, H. Schelin, M. B. Tsang, B. A. Remington, and J. Kasagi, Phys. Rev C **39**, 733 (1989).
5. L. Heilbronn, Ph.D. thesis, Michigan State University (1991).
6. J. Wilczynski and H. W. Wilschut, Phys. Rev. C **39**, 2475 (1989).

FEEDING OF BOUND-STATE POPULATIONS FROM NEUTRON-UNBOUND STATES FOR ^{14}N + Ag, E/A = 35 MeV REACTIONS

L. Heilbronn, F. Deak[a], A. Galonsky, C.K. Gelbke, J. Kasagi[b], A. Kiss[a], W.G. Lynch, T. Murakami[c], B.A. Remington[d], D. Sackett, H. Schelin[e], Z. Seres[f], and M.B. Tsang

The fact that the measured bound-state populations of intermediate-mass fragments (IMFs) are vulnerable to the effects of sequential feeding[1] is well established experimentally for intermediate-energy heavy-ion reactions (see Refs. 2 and 3, for example). In this report we present data that shows the amount of feeding into various IMF bound-state populations from neutron-unbound states from the reaction ^{14}N + Ag at E/A = 35 MeV. Using this data together with other sets of data of excited-state populations from the same reaction,[2-4] it is possible to put together a comprehensive set of data on the amount of feeding for this reaction.

Table 1 shows the percentage of a bound-state population that came from the decay of a neutron-unbound state. For example, 1.5 % of the ^{11}B bound-state yield at 15° was ^{11}B that came from the decay of the 3.388-MeV state in ^{12}B. The last six columns show the predictions for the amount of feeding according to a sequential feeding model calculation (see previous report), using initial temperatures of 2 MeV, 2.5 MeV, 3 MeV, 3.5 MeV, 4 MeV, and 5 MeV. Most of the data matches the model calculations for an initial temperature between 2.5 and 4 MeV. The model calculations could not match the data within uncertainties for one case, that being the feeding at 15° from the group of three levels around 7.5 MeV in ^{13}C to the ground state of ^{12}C.

The idea of sequential feeding was first introduced as a possible explanation for the discrepancy between population temperatures and spectral temperatures (see previous report). It was thought that accounting for the feeding would raise the measured population temperatures enough that they would agree with the spectral temperatures. Although feeding does raise the population temperatures, it is not enough to account for the difference. However, no attempt has been made to see what effect feeding has on the measured spectral temperatures. If the feeding is not constant as a function of kinetic energy, then correcting the IMF spectra for the feeding will change the slope of the spectrum, which in turn will have an effect on the deduced spectral temperature.

The dependence of the feeding on kinetic energy has been measured in detail for one case, that being the feeding from the 3.388-MeV state in ^{12}B to the ground state of ^{11}B. The top two plots in Fig. 1 show the fraction of feeding into ^{11}B from the 3.388-MeV state in ^{12}B at 15° and 31° as a function of ^{11}B kinetic energy. The solid lines show a convenient fit to the data. According to Table 1, the best value of the initial temperature that matches the feeding from both of the detected neutron-unbound states in ^{12}B is ~2.5 MeV. Using that initial temperature, the model predicts that ~33% of the yield of ^{11}B at 15° and 31° comes from feeding from all of the possible decay channels that end up in a bound state of ^{11}B. The lower two plots in Fig. 1 show the measured ^{11}B inclusive spectra at 15° and 31° (open symbols) and the spectra corrected for feeding (solid symbols) using a value of 33 % for total feeding. The dependence of the feeding on kinetic energy for all of the possible channels was assumed to be the same as the dependence for the one channel which was measured.

The solid lines through the corrected and uncorrected spectra in the lower plots of Fig. 1 indicate fits using the sum of two functions. One function was used to fit the deep-inelastic part of

Table 1 - Percent feeding from neutron-unbound states into their corresponding daughter-fragment inclusive yields at various angles. The uncertainty in the last significant digit(s) is enclosed in the parenthesis following the value of the feeding. The last 6 columns show predictions for the percent feeding from a sequential feeding calculation described in the text. The initial temperature used in the calculation is indicated in the column heading.

parent state	Θ	exp % feeding	model 2 MeV	model 2.5 MeV	model 3 MeV	model 3.5 MeV	model 4 MeV	model 5 MeV
^{7}Li(7.46)	15°	5.0(3)	2.1	5.1	8.7	12.3	15.4	20.5
^{7}Li(7.46)	31°	5.0(3)	2.2	5.1	8.7	12.3	16.0	21.6
^{7}Li(7.46)	64°	8.7(7)	2.2	5.3	9.0	13.2	16.5	21.6
^{8}Li(2.255)	15°	6.6(3)	1.2	2.8	4.7	6.8	8.6	11.7
^{8}Li(2.255)	31°	9.3(5)	1.2	2.8	4.8	6.8	9.0	12.3
^{8}Li(2.255)	64°	7.6(5)	1.2	2.9	5.0	7.4	9.3	12.3
^{9}Li(4.296)	15°	4.3(10)	0.5	1.2	2.1	3.1	4.1	5.8
^{9}Li(4.296)	31°	3.8(10)	0.5	1.2	2.1	3.1	4.1	5.8
^{8}Be(19.23)	15°	4.0(2)	1.5	3.6	6.1	9.0	11.9	17.3
^{8}Be(19.23)	31°	3.1(3)	1.5	3.6	6.2	9.0	11.9	17.1
^{10}Be(7.5)	15°	6.6(6)	2.3	5.7	9.5	13.1	15.7	18.7
^{10}Be(7.5)	31°	6.5(6)	2.4	5.7	9.7	13.1	16.3	20.0
^{10}Be(7.5)	64°	4.9(6)	2.4	5.8	9.9	14.0	16.8	20.0
^{10}Be(9.5)	15°	6.(2)	1.	3.	6.	9.	11.	14.
^{10}Be(9.5)	31°	4.2(12)	1.1	3.1	6.0	8.8	11.6	15.1
Σ^{10}Be	15°	12.(2)	3.	9.	15.	22.	27.	33.
Σ^{10}Be	31°	10.7(13)	3.4	8.8	15.6	22.0	27.9	35.1
^{11}Be(3.89)	15°	1.20(4)	0.13	0.34	0.61	0.91	1.21	1.75
^{11}Be(3.89)	31°	0.80(4)	0.13	0.34	0.62	0.91	1.23	1.82

parent state	Θ	exp % feeding	model 2 MeV	model 2.5 MeV	model 3 MeV	model 3.5 MeV	model 4 MeV	model 5 MeV
^{11}Be(3.89)	64°	1.3(3)	0.1	0.4	0.6	0.9	1.3	1.8
^{11}Be(3.96)	15°	1.10(14)	0.25	0.66	1.19	1.78	2.35	3.38
^{11}Be(3.96)	31°	0.60(11)	0.26	0.66	1.20	1.78	2.41	3.52
Σ^{11}Be	15°	2.69(14)	0.38	1.00	1.80	2.69	3.56	5.13
Σ^{11}Be	31°	1.30(12)	0.39	1.00	1.82	2.69	3.64	5.34
^{12}B(3.388)	15°	1.50(3)	1.15	2.03	2.55	2.82	2.80	2.56
^{12}B(3.388)	31°	1.60(4)	1.17	2.03	2.61	2.82	2.92	2.76
^{12}B(3.388)	64°	2.7(3)	1.2	2.1	2.7	3.1	3.0	2.8
^{12}B(3.76)	15°	1.70(18)	0.68	1.27	1.67	1.94	2.04	2.12
^{12}B(3.76)	31°	1.3(2)	0.7	1.3	1.7	1.9	2.1	2.3
Σ^{12}B	15°	3.20(18)	1.83	3.30	4.22	4.76	4.84	4.68
Σ^{12}B	31°	2.9(2)	1.9	3.3	4.3	4.8	5.0	5.0
^{13}C(6.86)	15°	2.7(8)	1.9	3.7	4.8	5.3	5.1	4.6
^{13}C(6.86)	31°	1.4(13)	1.9	3.7	5.0	5.3	5.5	5.4
^{13}C(7.5)	15°	16.(2)	4.	8.	11.	13.	12.	11.
^{13}C(7.5)	31°	12.(3)	4.	8.	12.	13.	13.	13.
^{13}C(9.5)	15°	1.50(8)	0.81	1.95	2.64	2.78	2.41	1.78
^{13}C(9.5)	31°	1.9(2)	0.8	2.0	2.7	2.8	2.7	2.2
^{13}C(9.5)	64°	3.5(12)	0.8	2.1	2.9	3.3	2.9	2.2
Σ^{13}C	15°	21.(2)	7.	14.	19.	21.	20.	18.
Σ^{13}C	31°	16.(3)	7.	14.	20.	21.	22.	20.
^{14}C(8.32)	15°	1.10(12)	1.25	2.10	2.51	2.72	2.68	2.56
^{14}C(8.32)	31°	1.6(2)	1.3	2.1	2.6	2.7	2.9	2.9

the two spectra at 15° and 31°, and it has the standard parameterization of a thermal moving source. The other function was used to fit the quasielastic part of the data, and it is the same function used to fit the quasielastic data in Ref. 5. Only the data at 15° and 31° was used for the fitting. The dotted lines in the lower plots show the contribution from the moving source for the uncorrected data, and the dashed lines show the contribution from the moving source for the corrected data. The value of the temperature of the moving source changed from 11.2 MeV before correcting for feeding to 14.0 MeV after the correction for feeding. The statistical uncertainty of the value of the temperature is less than 5%, in both cases. It appears, then, that correcting for feeding will increase the spectral temperature extracted from ^{11}B singles spectra, just as correcting for feeding will also increase the population temperatures. Based on these results, the effects of sequential feeding cannot account for the discrepancy between population temperatures and spectral temperatures.

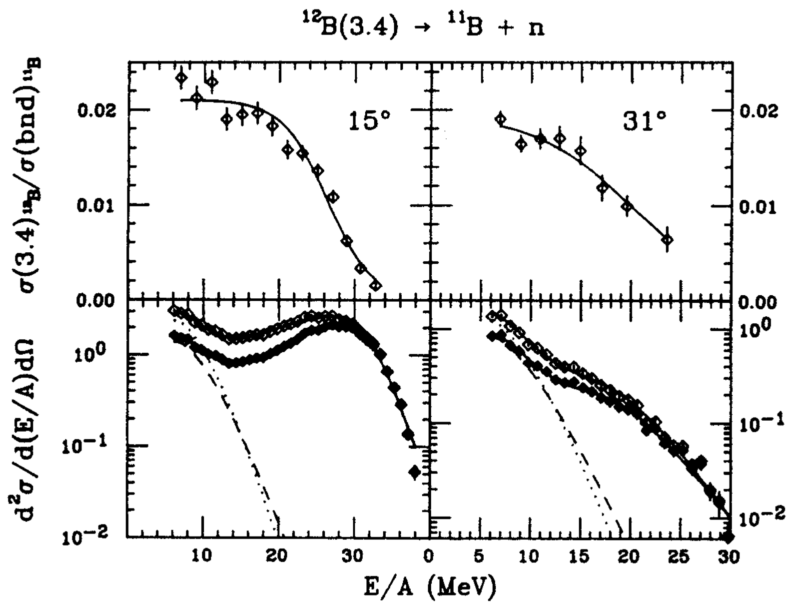

Fig. 1 - The upper plots show the ratio of the population of the 3.388-MeV state in ^{12}B to the bound-state population of ^{11}B as a function of ^{11}B kinetic energy. The solid lines are a fit to the data. The open symbols in the lower plots show the singles cross section of ^{11}B at 15° and 31° before correcting for feeding, and the closed symbols show the cross sections after the correction. The solid, dashed, and dotted lines in the lower plots come from fits described in the text.

a. Department of Atomic Physics, Eötvös University, Budapest 114, Hungary H-1088
b. Department of Physics, Tokyo Institute of Technology, O-Okayama, Meguro-Ku, Tokyo, Japan
c. Department of Physics, Kyoto University, Kitasherakawa, Kyoto 606, Japan
d. Lawrence Livermore National Laboratory, Livermore, California 94450
e. Centro Tecnico Aeroespacial and FAPESP, Brazil
f. Hungarian Academy of Sciences, KFKI, Budapest 114, Hungary H-1525

References

1. D. Hahn and H. Stöcker, Phys. Rev. C **35**, 1311 (1987).
2. C. Bloch, W. Benenson, A.I. Galonsky, E. Kashy, J. Heltsley, L. Heilbronn, M. Lowe, B. Remington, D.J. Morrissey and J. Kasagi, Phys. Rev. C **36**, 203 (1987).
3. D. Fox, D.A. Cebra, J. Karn, C. Parks, A. Pradhan, A. Vander Molen, J. van der Plicht, G.D. Westfall, W.K. Wilson and R.S. Tickle, Phys. Rev. C **38**, 146 (1988).
4. H.M. Xu, W.G. Lynch, C.K. Gelbke, M.B. Tsang, D.J. Fields, M.R. Maier, D.J. Morrissey, T.K. Nayak, J. Pochadzalla, D.G. Sarantites, L.G. Sobotka, M.L. Halbert and D.C. Hensley, Phys. Rev. C **40**, 186 (1989).
5. A. Kiss, F. Deak, Z. Seres, G. Caskey, A. Galonsky, B. Remington and L. Heilbronn, Nucl. Phys. **A499**, 131 (1989).